

Seismic Imaging Of an Intracrustal Deformation In the Northwestern Margin Of the South China Sea: the Role Of a Ductile Layer In the Crust

Xuelin Qiu¹, Haibo Huang², Frauke Klingelhöfer³, Yuhan Li², and Ping Wang²

¹Southern South China Sea Institute of Oceanology, Academia Sinica

²South China Sea Institute of Oceanology

³IFREMER

November 23, 2022

Abstract

The continental margins of the South China Sea (SCS) have undergone episodic rifting since the Cenozoic, and there are great divergences in processes of the crustal deformation and seafloor opening. In this work, we present a P-wave velocity model starting from north of Xisha Trough to Zhongshanan Basin in the northwestern SCS margin by modeling the ocean bottom seismometers data of a wide-angle seismic profile OBS2013-1. The results show that the crust thins symmetrically across the western Xisha Trough, from more than ~20 km at the flanks to ~10 km in the central valley where the sedimentary layers thicken to over 6 km. In the Zhongsha Trough closer to the deep basin, the upper crust is detached in a ~20 km wide region and the lower crust is intruded by volcanism and has seismic velocities increased by more than ~0.3 km/s. The volcanic intrusion was blocked by a shearing boundary between the brittle and ductile crust. A ~50 km wide ocean-continent transition region beneath the Zhongshanan Basin is underlain by ~6 km thick continental crust and shows high magnetic anomalies related to early stage magmatism and magnetized upper mantle. These observations, together with plate reconstructions based on gravity and magnetic analysis, suggest that the continental margin was deformed by crustal detachment and prominent magmatism that was followed by a rapid accretion of the oceanic crust.

1 **Seismic Imaging Of an Intracrustal Deformation In the Northwestern Margin Of the**
2 **South China Sea: the Role Of a Ductile Layer In the Crust**

3
4 **Haibo Huang^{1,3}, Frauke Klingelhoefer², Xuelin Qiu^{1,3,4}, Yuhan Li^{1,4}, Ping Wang^{1,3}**

5 ¹Key Laboratory of Ocean and Marginal Sea Geology, South China Sea Institute of Oceanology,
6 CAS, Guangzhou, P.R. China.

7 ²Department of Marine Geosciences, IFREMER, Plouzané, France.

8 ³Innovation Academy of South China Sea Ecology and Environmental Engineering, Chinese
9 Academy of Sciences, Guangzhou 510301, China

10 ⁴College of Earth and Planetary Sciences, UCAS, Beijing, P.R. China

11
12
13 Corresponding author: Xuelin Qiu (xlqiu@scsio.ac.cn)

14
15
16 **Key Points:**

- 17 • Intracrustal deformation that includes detached upper crust and ductile lower crust was
18 imaged across the Zhongsha Trough, a rift valley.
- 19 • Prominent magmatism in the OCT lead to a rapid onset of the embryonic oceanic crust
20 mixed with the highly fractured continental crust.
- 21 • Partially serpentinized upper mantle beneath the OCT indicates short-term fault activity
22 before the oceanic spreading.

23 **Abstract**

24 The continental margins of the South China Sea (SCS) have undergone episodic rifting since the
25 Cenozoic, and there are great divergences in processes of the crustal deformation and seafloor
26 opening. In this work, we present a P-wave velocity model starting from north of Xisha Trough
27 to Zhongshanan Basin in the northwestern SCS margin by modeling the ocean bottom
28 seismometers data of a wide-angle seismic profile OBS2013-1. The results show that the crust
29 thins symmetrically across the western Xisha Trough, from more than ~20 km at the flanks to
30 ~10 km in the central valley where the sedimentary layers thicken to over 6 km. In the Zhongsha
31 Trough closer to the deep basin, the upper crust is detached in a ~20 km wide region and the
32 lower crust is intruded by volcanism and has seismic velocities increased by more than ~0.3
33 km/s. The volcanic intrusion was blocked by a shearing boundary between the brittle and ductile
34 crust. A ~50 km wide ocean-continent transition region beneath the Zhongshanan Basin is
35 underlain by ~6 km thick continental crust and shows high magnetic anomalies related to early
36 stage magmatism and magnetized upper mantle. These observations, together with plate
37 reconstructions based on gravity and magnetic analysis, suggest that the continental margin was
38 deformed by crustal detachment and prominent magmatism that was followed by a rapid
39 accretion of the oceanic crust.

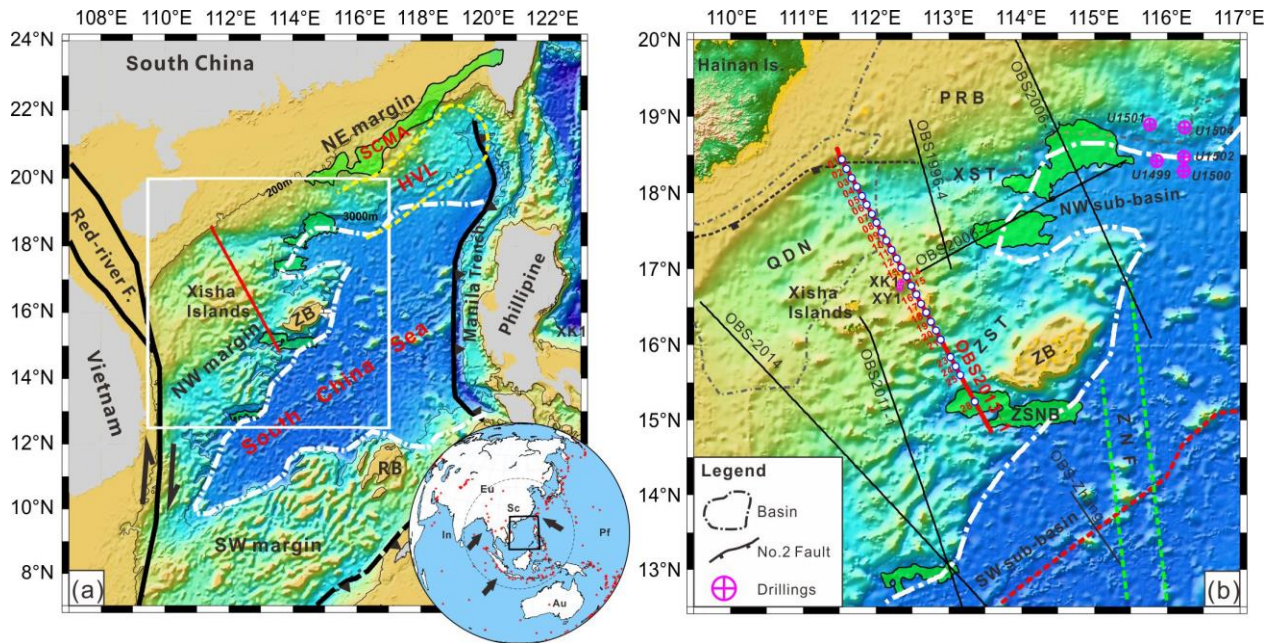
40 **1 Introduction**

41 The South China Sea (SCS) has been widely recognized as a Cenozoic marginal basin
42 developed from atypical magma-poor passive rifting ([Taylor and Hayes, 1983](#)). Depending on
43 lithologic composition, rheology and thermal structure of the continental lithosphere, passive
44 margins can undergo progressive extension in variable styles of crustal deformation ([Huisman
45 and Beaumont, 2014](#)). Over the years, geophysical surveys have revealed an asymmetrical

46 conjugate pattern and the depth-related lithospheric extension of the margins in the SCS (Franke
47 et al., 2014; Huismans and Beaumont, 2014; Huang et al., 2019). However, the rupture mode of
48 the continental crust and the growing processes of the oceanic crust are still highly controversial.
49 In 2017, the 367/368 IODP drillings have been conducted in deep water (> 3000 m; Fig. 1) at
50 the edge of the northern margin of the SCS to reveal the nature of the transitional structures from
51 continent to ocean (Jian et al. 2018; Sun et al. 2018). The coring data suggest that the SCS has
52 experienced fast lithospheric extension without mantle exhumation (Larsen et al., 2018), very
53 different from the well-established findings along the Atlantic Ocean margins (Dean et al., 2000).
54 In addition, early-stage magmatism prior to steady-state seafloor accretion was detected
55 overlying hyper-thinned continental crust (~8 km thick) and showing an east to west propagation
56 based on interpretation of reflection seismic profiles (Larsen et al., 2018). Accordingly,
57 interlayer decoupling in the lithosphere could have been facilitated when the pre-rupture
58 magmatism heating up and reducing the crustal viscosity (Franke et al., 2014).

59 The lithology measurements of the sampled rocks should be implemented combining
60 closely with deep structure detection such as the geophysical exploration. The obtained seismic
61 structures will provide an explanation for the rheological behavior of the continental crust (e.g.,
62 the weak zones and interlayer decoupling) that finally determines the transition pattern from
63 rifting to rupturing (Huismans and Beaumont, 2014). Moreover, original architecture and thermal
64 structure of the crust usually evolved during poly-phased extension (Brune et al., 2014), and it
65 requires a comparison of the deforming expressions in time and space. In this work, we present a
66 P-wave velocity model from a wide-angle seismic survey starting from the slope area in the
67 northwestern margin of the SCS to the south of the Zhongsha Bank (Macclesfield Bank; Fig. 1b).
68 Seismic travel times were modeled to image the rift-related structures e.g. brittle/ductile behavior

69 of the continental crust, and thus to provide further insights into the crustal deformation during
 70 rifting. The crusts show a regional deformation pattern in the failed rifts, and hyper-thinned
 71 continental crust in the ocean-continent transition zone (OCT) is overprinted by early-stage
 72 magmatism, which is in good agreement with the shallow lithology measurements from IODP
 73 drilling.



74
 75 Fig. 1 Location map showing the study region in the South China Sea. (a) High magnetic
 76 anomalies close to the slopes and in the northeastern (NE) margin are both represented by green
 77 masked polygons. Distribution of the high velocity layer (HVL) is enclosed by dashed yellow
 78 line. The dashed white line is the continent-ocean boundary (COB) referring to Li and Song
 79 (2012). SCMA – South China Magnetic Anomalies along the NE margin of the SCS; RB - Reed
 80 Bank. The inset shows the tectonic setting of the SCS, in which, Eu is the Eurasia Plate, In is the
 81 India Plate, Au is the Australian Plate, Pf is the Philippine Plate and Sc is the South China block.
 82 (b) Map showing the seismic profiles and the IODP drilling sites. In which, OBS2013-1 is
 83 marked by a red line and the circles along the line represent OBS locations. Other profiles are

84 labeled and shown as black lines, OBS2011-1 (Huang et al., 2019); OBS-2014 (Pichot et al.,
85 2013); OBS1996-4 (Qiu et al., 2001); OBS2006-1 (Wu et al., 2011); OBS2006-2 (Ao et al.,
86 2012); and OBS-Zhang (Zhang et al., 2016). The dashed red line is the aborted spreading ridge.
87 QDN - Qiongdongnan Basin; PRB - Pearl River Mouth Basin; XST - Xisha Trough; ZB -
88 Zhongsha Bank; ZST - Zhongsha Trough; ZSNB - Zhongshanan Basin; ZNF - the Zhongnan
89 Fracture Zone.

90 **2 Geological Setting**

91 The SCS margins developed along a NE-strike divergent setting due to rollback of the
92 subducted Paleo-Pacific plate in the Late Mesozoic (Taylor and Hayes, 1983). Long-lasting
93 continental rifting of the margins started in the latest Cretaceous to Early Paleocene (~65 Ma)
94 and ceased prior to the progressive seafloor opening from ~32 Ma to ~15 Ma (Briais et al., 1993;
95 Larsen et al., 2018). As a result, the SCS evolved into segmented sub-basins (Taylor and Hayes,
96 1983), and the margins also show along-strike deforming patterns of the continental crust
97 (Franke et al., 2014; Hayes and Nissen, 2005). For the northern margin, the eastern segment is
98 characterized by the presence of a high velocity layer (HVL; the location is shown in Fig. 1a)
99 underlying either hyper-thinned continental crust or separated upper crust (McIntosh et al., 2014).
100 A remarkable high magnetic anomaly belt in the northern margin (SCMA) has long been
101 discussed and considered as a remnant of Mesozoic subduction arc (Wan et al., 2017). In
102 comparison, the western section exhibits a normally extended continental crust (Hayes and
103 Nissen, 2005), alternating with aborted rifts and rigid blocks in broad region. However, volcanic
104 relics associated with the Mesozoic subduction have also been recognized along the northwestern
105 and its conjugate margins, characterized by sporadically distributed high-amplitude positive
106 magnetic anomalies (Li et al., 2018). Whether or not the HVL exists in these areas is debated, as

107 several wide-angle seismic surveys reported its absence (Wu et al., 2011; Qiu et al., 2001),
108 whereas a few reflection seismic surveys and gravity modeling revealed scattered HVLs (Pichot
109 et al., 2013; Qiu et al., 2013). Besides, performance of the ductile crustal layers also shows a
110 high discrepancy between different investigations, in terms of the amount of stretching within the
111 crust (Zhu et al., 2016).

112 The NW margin of the SCS, bordered by the Red River Fault Zone to the west (Fig. 1a),
113 preserves lithospheric deformation features from episodes of the rifting processes. Basin analysis
114 has revealed a zonal distribution of the tectonic stresses (Ren and Lei, 2011), including the
115 collision-induced extrusion of the Indochina block in the west that has formed pull-apart basins
116 like the Yinghai basin, Zhongjiannan basin and east of the Qiongdongnan Basin (Fig.1b). For
117 the eastern part where the Xisha Islands (Paracel Islands) and the Zhongsha Trough are located,
118 grabens and horsts were mainly shaped by normal and low-angle faults in extension and
119 characterized by ductile shearing of the continental crust (Ren et al., 2014). Wide-angle seismic
120 surveys have imaged highly extended continental crust with a thickness of less than 8 km along
121 these troughs and basins, e.g., the Xisha Trough, which represents an aborted rift valley (Qiu et
122 al., 2001). Seismic surveys using seafloor cables have identified strong post-spreading volcanism
123 and hydrothermal activity along the rift faults, while the syn-rift igneous rocks are rarely visible
124 above the crust (Gao et al., 2016).

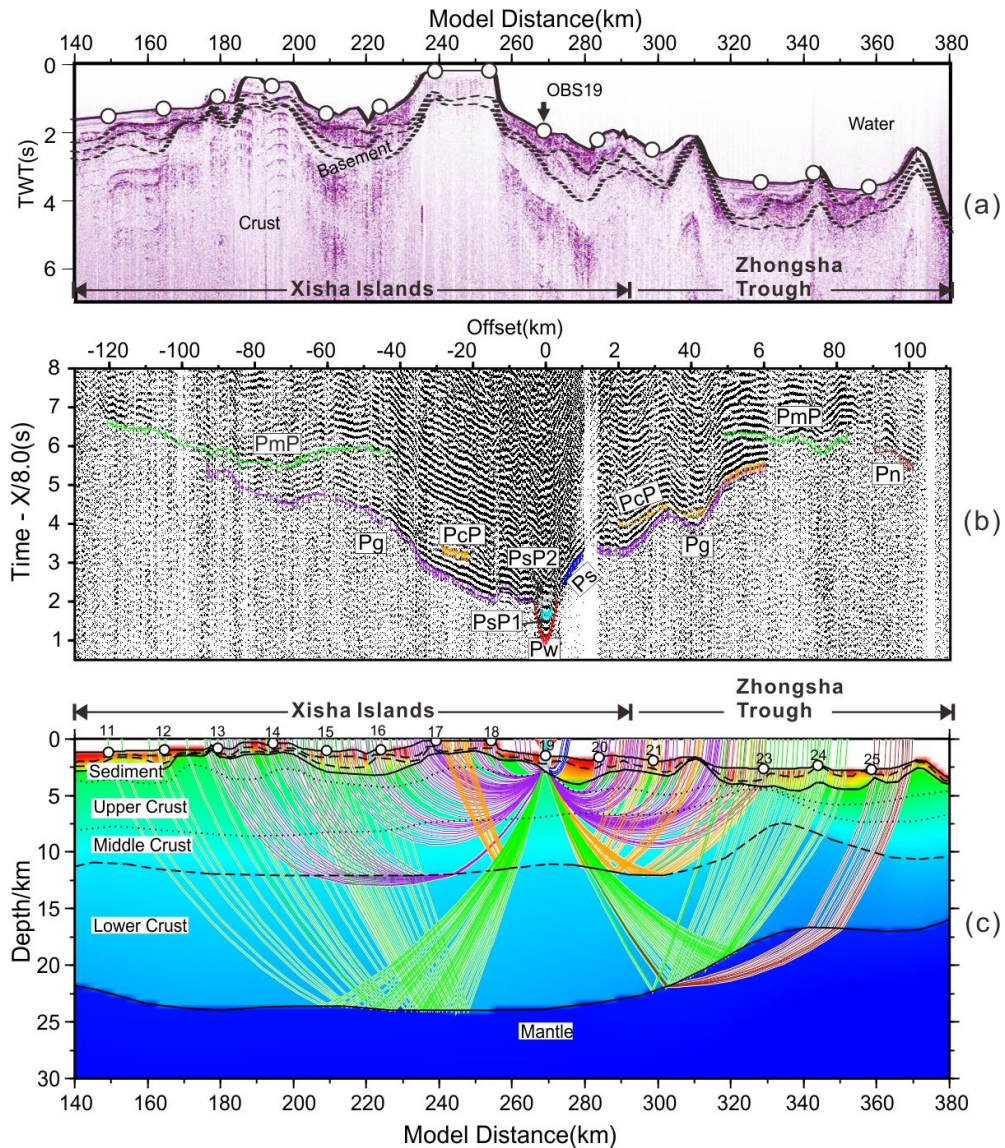
125 Tectonic subsidence is considerably delayed for more than 10 Myrs due to ongoing rifting or
126 rising asthenospheric material along the NW margin (Franke et al., 2014), and the uplifted
127 basement thus provided a good place for growth of the reefs around the Xisha Islands (Ma et al.,
128 2011). Controversy still exists mainly concerning the basement nature and age beneath the
129 islands. Several boreholes have been drilled on the islands for dating and classifying the

130 basement rocks (e.g. XY1 and XK1 in Fig. 1b). Precambrian granitic rocks have been drilled and
131 dated at the borehole XY1 (Zhang 1991). Nevertheless, results from the latest coring data from
132 the borehole XK1 indicate that the basement rocks are constituted by Late Mesozoic igneous
133 rocks, possibly representing the widespread volcanic intrusions over the SCS due to the Paleo-
134 Pacific subduction (Zhu et al., 2017). Volcanic rocks dredged near the Zhongsha Bank in the east
135 of the Xisha Islands were also dated with a Late Mesozoic age (Jin 1989). Geophysical surveys
136 show that the Zhongsha Bank consists of extended continental crust with a thickness of more
137 than ~20 km (Wu et al. 2011). Localized crustal deformation and magmatism was prevailing at
138 the edge of these continental banks, as indicated by reflection seismic surveys and analog
139 modeling on stretching mechanism of the rigid blocks (Ding and Li 2016).

140 **3 Data and Methods**

141 3.1 Data acquisition and seismic phases

142 In April and May 2013, the ‘Shiptime Sharing Project of NSFC’ conducted a geophysical
143 cruise across the Xisha Islands using the R/V ‘Shiyan 2’. During the cruise, a ~500 km long
144 wide-angle seismic profile (OBS2013-1; Fig. 1b) striking NW-SE was acquired starting from
145 west of the Xisha Trough and reaching the south of the Zhongsha Bank and coinciding with a
146 multi-channel reflection seismic profile of four streamers. Thirty ocean bottom seismometers
147 (OBS) spaced at ~15 km were deployed, among which 25 OBSs were successfully recovered and
148 provided useful data. Four air guns with a total volume of ~98 L were deployed ~30 m behind
149 the vessel and shot every 120 s, leading to ~300 m shot spacing at a ship speed of ~5.0 Kn.



150

151 Fig. 2 Seismic modeling of the OBS data. (a) A segment of the reflection seismic data section.

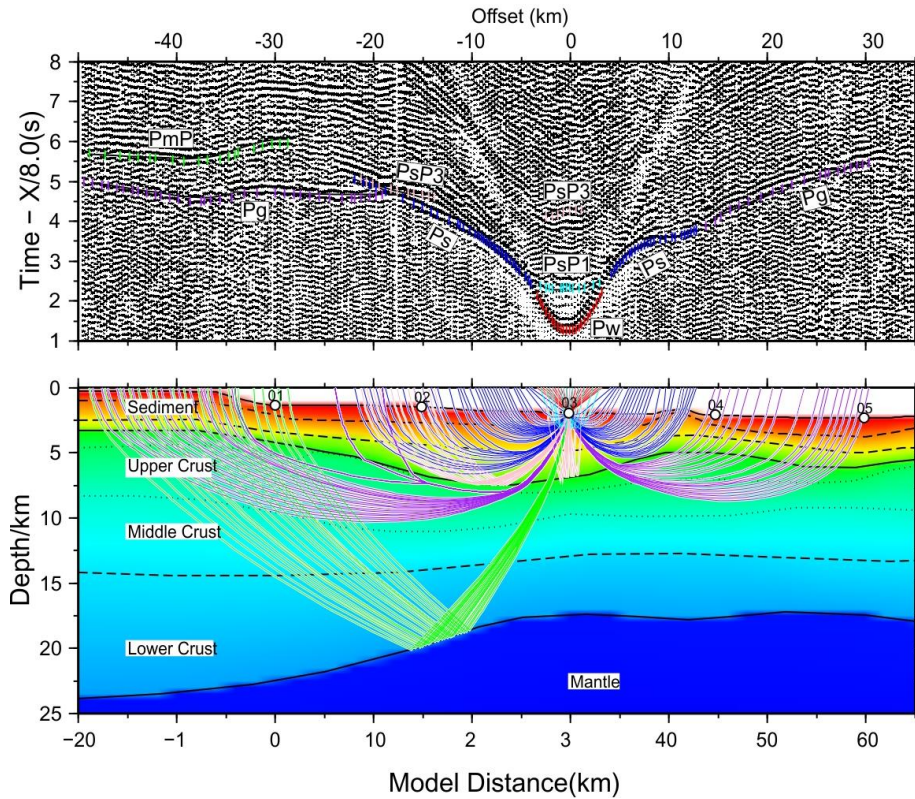
152 The white circles mark locations of the OBSs. The solid line and the dashed lines respectively

153 represent the seafloor and the sedimentary interfaces from the forward modeling. (b) Seismic

154 section of OBS19, overlain by the calculated travel times in different colors. The reduced

155 velocity is 8.0 km/s. Location of OBS19 is shown in Fig.1b. (c) A segment of the forward

156 velocity model. Seismic ray paths are shown in colored lines.



157

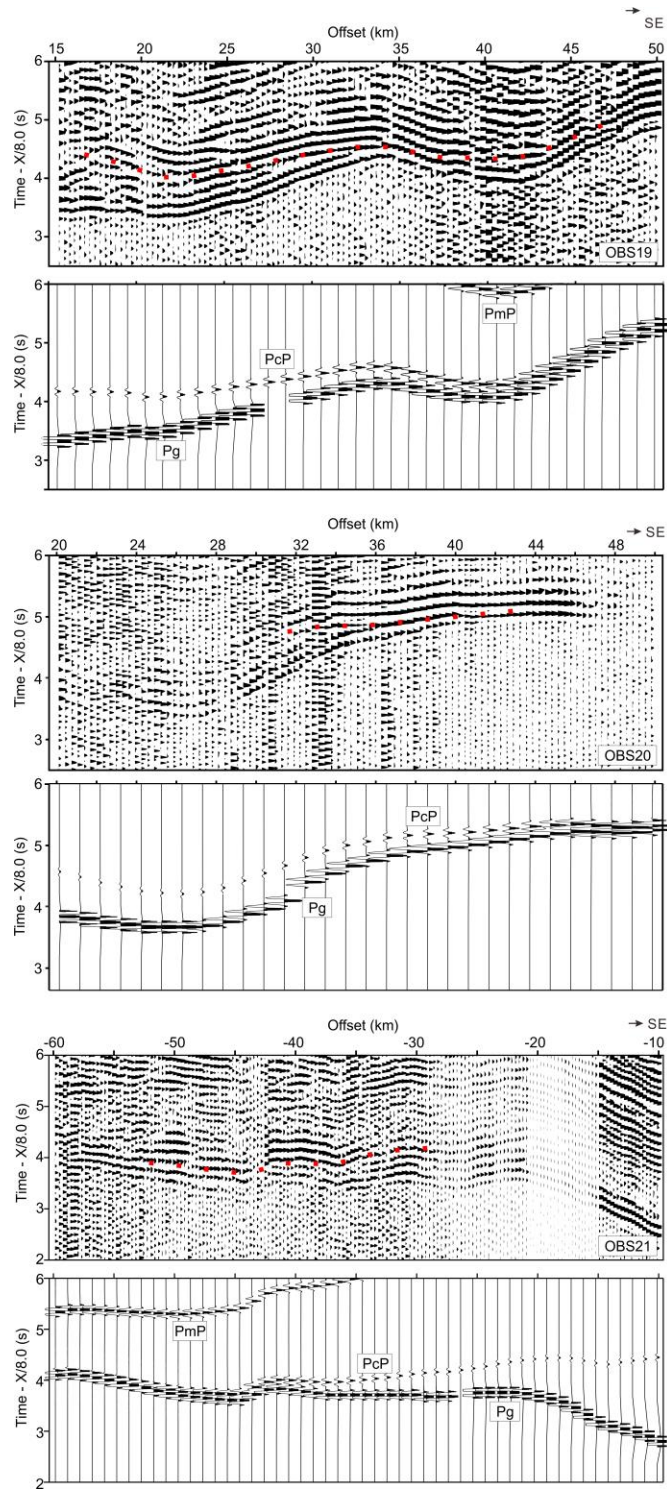
158 Fig. 3 Seismic modeling of the data from OBS03. The reduced velocity is 8.0 km/s. Location of
 159 OBS03 is shown in Fig.1b. Seismic ray paths are shown in colored lines.

160 The raw seismic data were corrected for the clock-drift, and instrument positions were
 161 relocated by fitting the direct water-wave traveltimes using the least-square method (West et al.,
 162 2001). A spectrum-whitening deconvolution was used to remove the bubble reverberations and
 163 highlight the primary arrivals. Automatic gain of the seismic amplitudes and zero-phase band-
 164 pass filter (3-15Hz) were also applied to further enhance the seismic signals. The reflection
 165 seismic data were processed following basic steps, including trace sorting, filtering and
 166 automatic gain. The OBS sections show clear refracted phases traveling through the sediments
 167 (Ps), the crust (Pg) and the upper mantle (Pn). Sedimentary reflections (PsP1, PsP2) as well as
 168 reflections from top basement (PsP3), mid-crustal interface (PcP) and the Moho (PmP) were also

169 identified (Fig. 2 - 4). A total of 10346 arrivals including 5856 refractions and 3992 reflections
170 were finally picked.

171 3.2 Velocity modeling

172 The P-wave velocity structures were constraint jointly by forward modeling (Zelt and Smith,
173 1992) and tomographic inversion (Korenaga et al., 2000) of the seismic data. A combination of
174 both approaches allows drawing a user-independent velocity model including as much available
175 information as possible (Huang et al., 2019). The forward modeling was proceeded using the
176 layer-stripped method to decrease the misfits between the picked and calculated traveltimes (see
177 Fig.3-4 and the supplementary material). Firstly, a 3-layer sedimentary model with variable
178 velocities in a range of 1.7-4.5 km/s below the seafloor was constructed by forward modeling of
179 the Ps and PsP phases. Velocities whin the sediments decide the seismic phase morphologies,
180 which is more easily identified when the sedimentary layer is less fluctuated, as shown in the left
181 branch of Fig.3. Velocity boundaries between the sedimentary layers as well as the basement
182 were converted from depth to two-way traveltime and match the reflection seismic data (Fig. 2a).
183 Secondly, tomographic inversion of the crustal structures was implemented using Pg and PmP
184 phases, taking the sediments as input information. Finally, the inversion model was further
185 revised by forward modeling to prevent over interpretation of the data. Velocity boundaries
186 within the crust were continuously traced by the PcP phases (Fig. 4), thus providing information
187 for imaging internal structures of the crust (Fig. 2). The identification and modeling of the inter-
188 crustal interface were verified by calculating the synthetic waveforms based on zero-order
189 asymptotic ray theory (Zelt and Ellis, 1988). Basically, the theoretical PcP phases with relative
190 higher amplitudes correspond to the real phases that are easy to pick (Fig. 4). The velocities of
191 the upper mantle were modeled based on the Pn phases once the crust was well constraint.



192

193 Fig. 4 The PcP phases recorded in OBS19, OBS20 and OBS21. Red dotted lines denote the

194 picked PcP phases. For each OBS, the upper panel shows the real seismic profile, while the

195 lower panel shows the synthetic one based on the velocity model and the calculated traveltimes.
196 The reduced velocity is 8.0 km/s.

197 **4 Results**

198 Modeling of the OBS2013-1 data resulted in a velocity model showing sedimentary and
199 crustal structures along the complete NW margin to a depth of 30 km (Fig. 5b). The sedimentary
200 and crustal structures will be discussed together with the interpretation of the reflection seismic
201 data. This helps to better understand the deforming pattern of the continental crust as well as the
202 magmatic activity along the margin. The modeling errors are discussed below, and main features
203 of the velocity model are described according to the major tectonic units.

204 4.1 Error calculations of the velocity model

205 The tomographic model was parameterized in a grid mesh with node spacing of 0.5 km in
206 the horizontal dimension and 0.05-0.25 km in the vertical dimension increasing downward. The
207 Moho and the inter-crustal boundary were both defined with uniform 1 km spacing. Smoothing
208 weighting factors for the velocity and depth were set to 200 and 20 after conducting a set of trials
209 to avoid artifacts in the velocity models. Checkerboard tests of the model resolution were applied
210 to the final tomographic model (Fig. 6a-c) (Korenaga et al., 2000). A rectangular perturbation
211 pattern of 8% of the velocities, with a horizontal cell-size of 25 km and vertical cell-size 6 km
212 can be successfully recovered (Fig. 6b and Fig. 6c). More details can be revealed in the inversion
213 model (Fig.6d) than the forward one (Fig.5c) mainly for the upper crust, and the velocity
214 perturbation and sizes in both models are within the identifiable range as indicated by the
215 checkerboard tests. The uncertainty of the layered structures in the final forward model was
216 assessed using a Monte Carlo approach (VMONTECARLO; Loureiro et al., 2016). 500,000
217 random models were constructed and evaluated to produce a global uncertainty map of the

218 velocity and depth nodes (Fig. 7). Generally, the velocity uncertainty varies between ± 0.3 km/s
219 while the Moho-depth uncertainty ranges between ± 1 km. Large velocity uncertainty values were
220 located near the Moho and the inter-crustal interface, indicating either a poor ray coverage or a
221 strong trade-off between the depth and velocity at the velocity boundary (Loureiro et al., 2016).

222 4.2 Structures beneath the Xisha Trough and its flanks

223 A 3- to 6-km-thick Cenozoic sedimentary sequence was imaged along the west Xisha
224 Trough, composed of three layers with velocities of 1.7-4.5 km/s and velocity discontinuities
225 between 0.1-0.5 km/s across the interfaces. The top of the basement is characterized by a long-
226 wavelength morphology variation across the section, showing a progressive deepening toward
227 the shelf foot. This results in a thickened sedimentary layer and formation of a ~ 70 km wide half-
228 graben. A basement high is located at the trough center and overlain by a seamount with average
229 seismic velocity of ~ 3.5 km/s. For comparison, the sedimentary cover of the Xisha Islands is
230 much thinner (~ 2.5 km) and overlies a relative shallow basement at ~ 3 km depth.

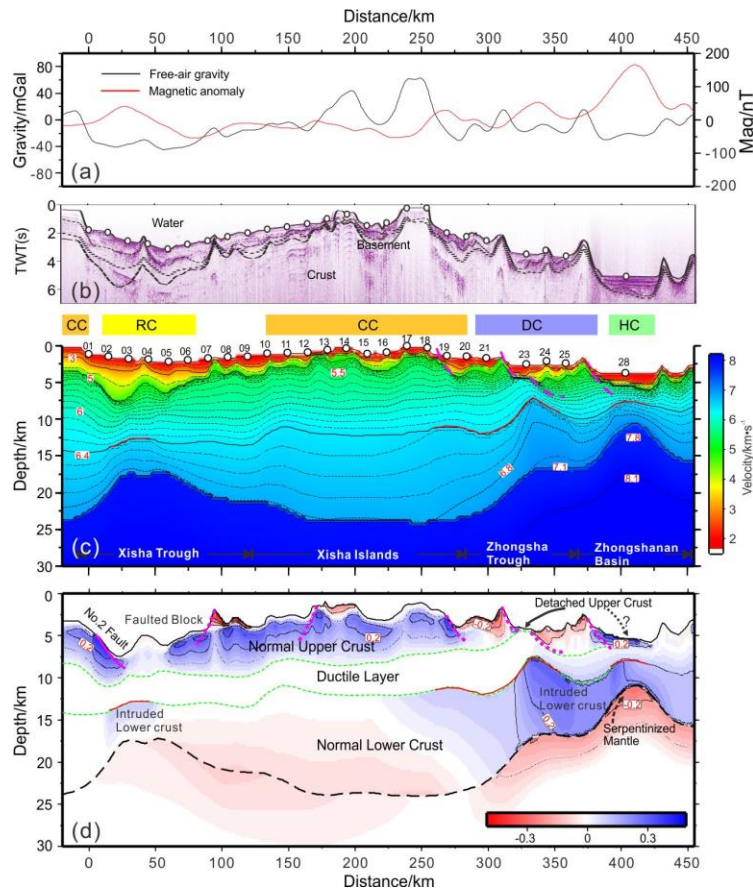
231 The Moho is located deeper than 22 km below the shelf at the Xisha Islands, and rises
232 progressively toward the Xisha Trough to ~ 17.5 km. The P-wave velocity increases from 5.0
233 km/s at the basement's top to ~ 6.8 km/s at the bottom of the crust. A velocity boundary near the
234 isovelocity contour of 6.4 km/s was sampled by the PcP phases in a 30-km wide area, and the
235 velocity contrast across this boundary is ~ 0.1 km/s.

236 4.3 Zhongsha Trough and Zhongshanan Basin

237 A series of horsts and grabens developed across the Zhongsha Trough, with basement highs
238 and intermediately thick sedimentary deposits (~ 3 km). Velocities at the basement top vary
239 between 5.0 and 5.6 km/s. The Moho becomes shallower rapidly from ~ 23 km in the Xisha

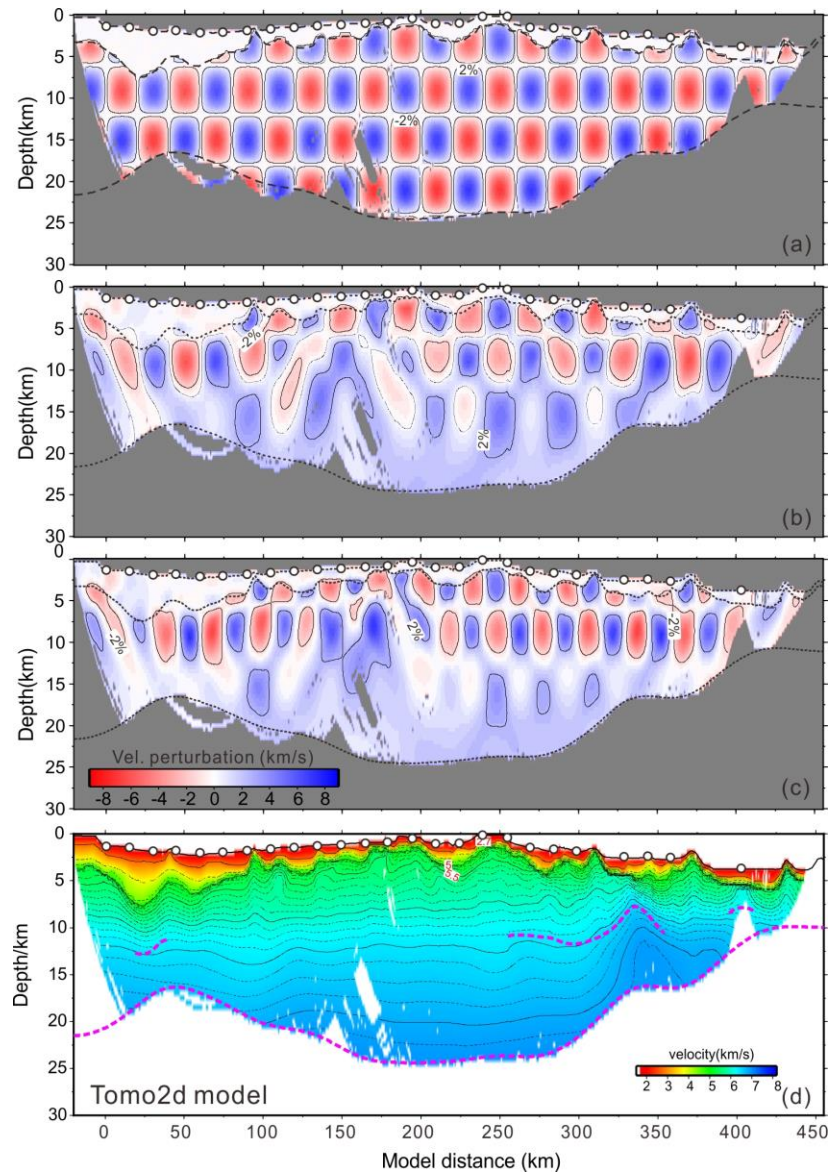
240 Islands to ~15 km and ~11 km respectively in the Zhongsha Trough and the Zhongshanan Basin,
241 over a distance of ~100 km. The crustal thickness is ~6 km in the Zhongshanan Basin, where a
242 lens-shaped layer less than 2 km thick was modeled by seismic velocities of ~3.8 km/s on top of
243 the basement. It was also identified in the reflection seismic section and corresponds to a high
244 positive magnetic anomaly (~170 nT; Fig. 5a and Fig. 9c).

245 The crustal velocities also show a complex variation across the Zhongsha Trough. The
246 upper crust, taking the 6.4 km/s isovelocity line as the lower boundary, is stretched to be less
247 than 5 km thick and accompanied by uplifted lower crust. Accordingly, velocity in the lower
248 crust increases by ~0.3 km/s forming a sharp velocity contrast across the boundary (Fig.5c-d),
249 which can be continuously traced in a range of ~90 km by the PcP phases (Fig. 4). A similar
250 inter-crustal velocity boundary is located beneath the Zhongshanan Basin, where the velocity
251 contrast is slightly reduced to 0.1-0.2 km/s (Fig.5c-d). The uppermost mantle beneath the basin
252 shows a lower average velocity at ~7.7 km/s than the adjacent areas, in a horizontal range of ~50
253 km and vertical depth of more than 3 km from the Moho.



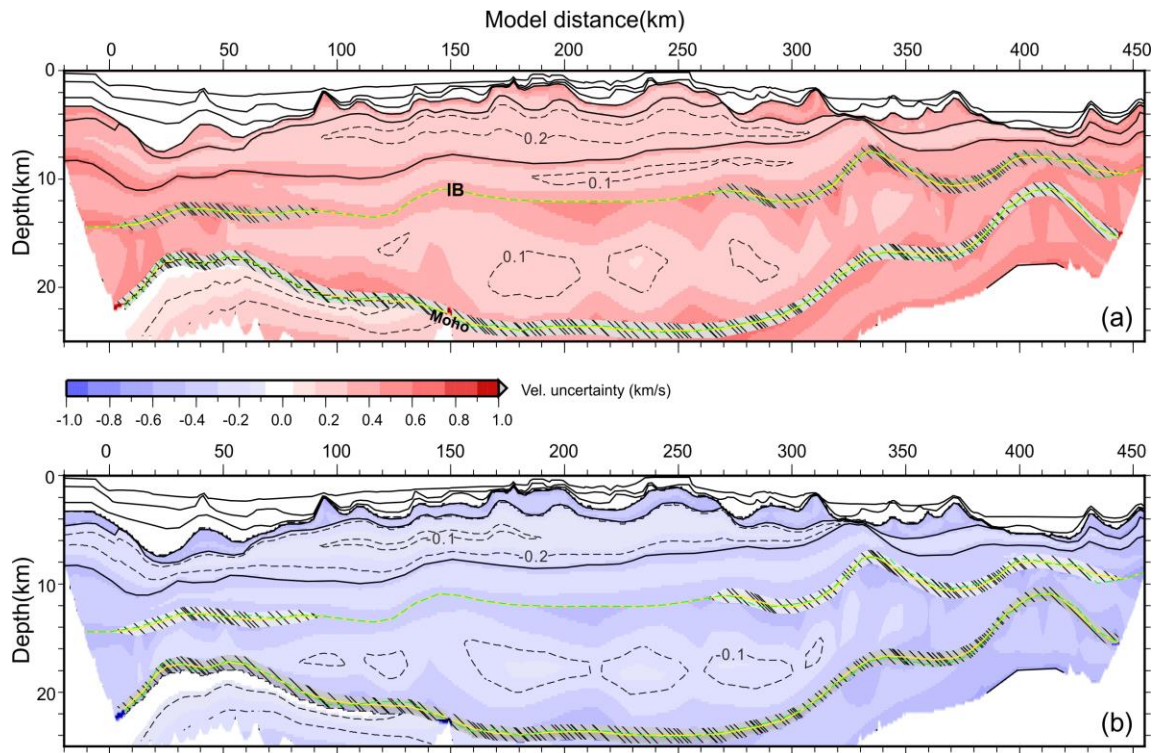
254

255 Fig. 5 Final seismic model and velocity perturbation of the OBS2013-1. (a) Gravity anomaly
 256 (black line) and magnetic anomaly (red line). (b) Reflection seismic data section. (c) P-wave
 257 velocity model. CC - continental crust; RC - rift valley crust; DC - detached crust; HC - hyper-
 258 thinned crust. (d) Velocity perturbation in the crust shown in positive (blue) and negative (red)
 259 values. The thick red lines show the faults cutting the basement. The green lines outline the
 260 ductile layer between the normal upper crust and the lower crust. The black dashed line shows
 261 the Moho, while the thin red solid lines show the constraint inter-crustal interface.



262

263 Fig. 6 Results of the checkerboard tests for the velocity model. The amplitude of the velocity
 264 perturbation is 8%. (a) Original perturbed forward model, with anomaly size in $25 \text{ km} \times 6 \text{ km}$. (b)
 265 Recovered anomalies in $25 \text{ km} \times 6 \text{ km}$. (c) Recovered anomalies in $15 \text{ km} \times 6 \text{ km}$. (d) The
 266 tomographic inversion model. In which, the purple dashed lines are the inverted velocity
 267 interfaces.



268

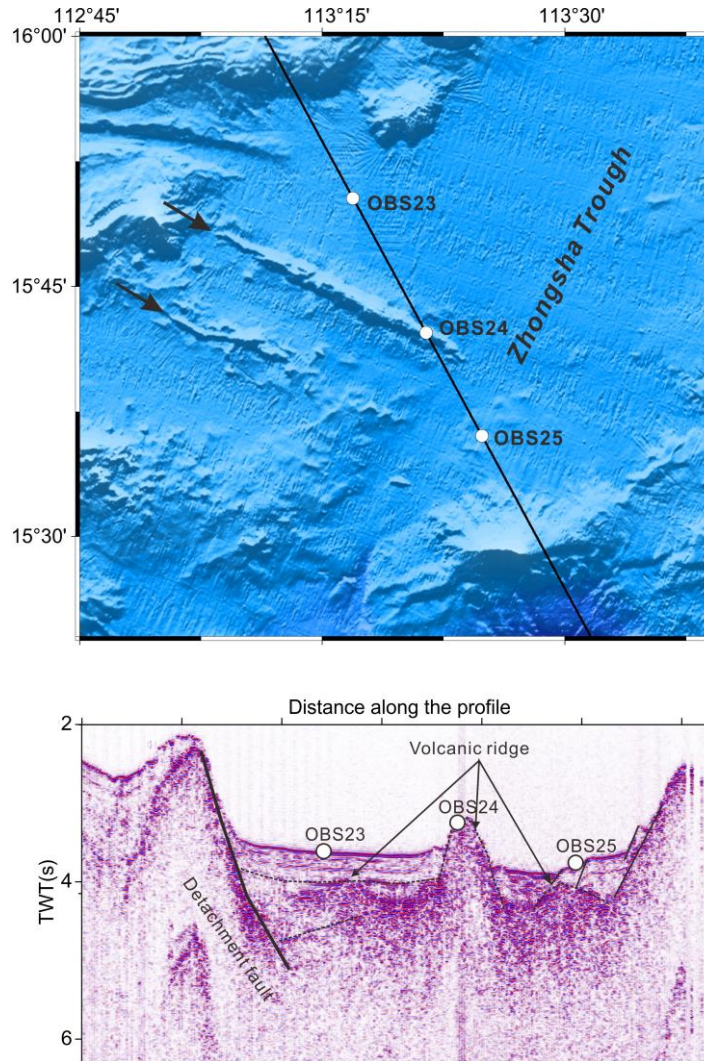
269 Fig. 7 Monte Carlo uncertainty tests of the forward model. The hatched areas at the intra-crustal
 270 boundary (IB) and the Moho denote the depth uncertainties for the both boundaries. Dashed
 271 yellow and green lines, respectively, indicate the best random model's and the forward model's
 272 IB and Moho. (a) Positive velocity uncertainties of the forward model. (b) Negative velocity
 273 uncertainties.

274 5 Discussion

275 5.1 Intracrustal deformation and identification of a ductile layer

276 The velocity model provides direct evidence for the intracrustal deformation, as the inter-
 277 crustal boundary (Fig. 7a) and the Moho have been precisely mapped. The model can be divided
 278 into four distinct sections according to these crustal structures (Fig. 5c). The Xisha Islands and
 279 the shelf area are identified as continental blocks that have experienced weak and uniform
 280 stretching. The crustal thickness (~22 km) is in good agreement with the values derived from the

281 receiver functions on the islands (Huang et al., 2011). Along the western Xisha Trough, the crust
282 has been stretched to be as thin as ~10 km beneath the half graben that is named the Songnan
283 Sag of the Qiongdongnan Basin (Ren et al., 2014). Between OBS01 and OBS02, the top
284 basement shows an increased velocity by ~0.5 km/s compared to both sides (Fig. 5d), which is
285 also proposed by Qiu et al. (2013). In earlier work, it was proposed to represent a detachment
286 fault that shaped the half graben within the basin (Ren et al. 2014). This fault may not only
287 contribute to the gravity anomaly identified along our model (Fig. 5a), but also the associated
288 variation of the seismic velocity (Fig. 5d). A similar complex basement shape was also presented
289 by Qiu et al. (2001), and the basement high in the center can be interpreted as a rotated
290 continental block related to a rollover anticline (Ren et al., 2014). Using an initial crustal
291 thickness of 30 km, it corresponds to a stretching factor β of 3.0 that is less than the value
292 calculated from the Xisha Trough ($\beta \sim 3.8$; Qiu et al., 2001), probably due to the westwards
293 propagated continental rifting.



294

295 Fig. 8 Enlarged topography of the Zhongsha Trough (top), where the white circles are OBSs and
 296 the two arrows show the volcanic ridges. (Bottom): reflection image of the volcanic
 297 ridges/intrusion.

298 In the southern part of the profile, a prominent rise of the Moho and a relatively shallower
 299 basement than the north are modeled, reflecting the delayed subsidence of the NW margin of the
 300 SCS (Franke et al., 2014). Instead of a wide rift valley like the Xisha Trough, a series of half
 301 grabens distributed along this region bordered by seaward dipping faults and corresponding
 302 basement highs were imaged. These faults extend down to depths of approximately 7 km where

303 the velocity shows high perturbations and distinctive gradients (Fig. 5c and Fig. 5d). Strikingly,
304 the crust with velocity lower than 6.0 km/s is dismantled along a small window about 20 km
305 wide in the Zhongsha Trough (near OBS23), with rotated basement on both flanks that might
306 also represent rollover structures. Magnetic profiles show anomalies of ~50 nT along the
307 Zhongsha Trough (Fig. 5a), following closely these faults and rollover structures. In contrary to
308 the SCMA, this weak-to-intermediate anomaly might correspond to metamorphic basements or
309 fault-controlled volcanic ridges as shown in the topography (Fig. 8).

310 The top boundary of the lower crust can be imaged in an extended range, buried at a depth
311 of ~13 km across the Zhongsha Trough (Fig. 5c). Previous long-cable seismic surveys also
312 imaged reflectors at around ~15 km depth in the northern and western SCS margins, where the
313 listric faults sole out and which may represent the brittle-ductile transition zone (Lester et al.,
314 2014). By considering the brittlely deformed upper crust along the detachment fault, we propose
315 that a ~5 km thick ductile layer exists beneath the upper crust, separated from the lower crust by
316 a shearing surface (Fig. 5c-d). Reflected phases from the top boundary of this ductile layer were
317 not detected, possible due to a small seismic impedance contrast or a low resolution of the OBS
318 data. Franke et al. (2014) suggested that the ductile layer might be the shallower portion of the
319 lower crust, which is important for compensating the upper crustal extension. Shi et al. (2002)
320 have also presented a similar rheological stratification across the Xisha Trough based on the
321 thermal modeling, in which the lower crust shows high rheological weakness. Thickness of the
322 lower crust beneath the shearing surface appears to be 2-3 km more under the Zhongsha Trough
323 than the blocks on both sides (Fig. 5c). The bottom of the lower crust shows slightly increased
324 velocities of up to 7.1 km/s (Fig. 5c-d). Similar to the Kenya and Baikal rifts, this may indicate
325 magmatic additions during rifting (Thybo and Nielsen, 2009). From our model, the highly

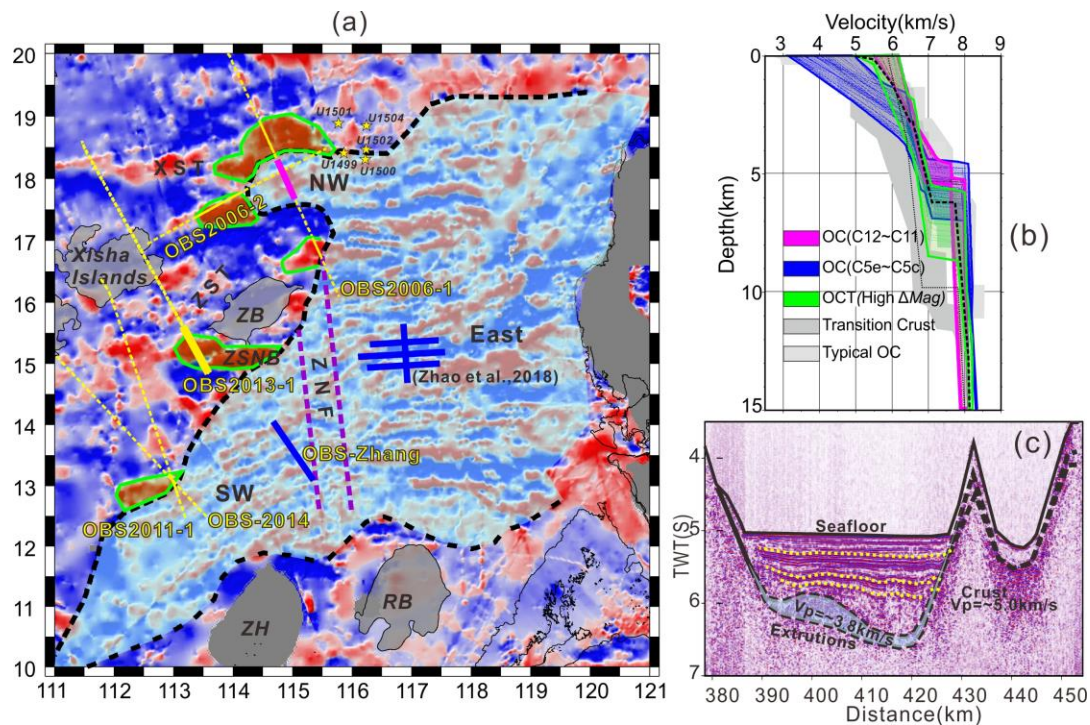
326 reflective top of the lower crust indicates a prominent velocity/density contrast, which could
327 have been enhanced by a front of intruded sills blocked at the ductile boundary (Fig. 5d and Fig.
328 10c, d). Nevertheless, the average velocity of the lower crust of ~ 6.8 km/s is much lower than the
329 HVL (possibly corresponding to volcanic underplating) in the NE margin (Wan et al., 2017),
330 reflecting different extents or sources of the volcanic activities.

331 5.2 Hyper-thinned continental crust in the OCT

332 A stretching factor of ~ 5 can be calculated in the Zhongshanan Basin off Zhongsha Bank,
333 representing a possible location for breakup of the continental crust (White and McKenzie, 1989).
334 In order to determine the nature of the crust, averaged velocity-depth profiles were extracted
335 from the velocity model (Fig. 9b). It shows that the crustal velocities and thickness are in good
336 agreement with those from typical Atlantic oceanic crust (White et al., 1992). A two-layer
337 structure, separated by a clear velocity step, represents the oceanic layer 2 and layer 3. However,
338 the magnetic anomaly in this area does not show the pattern with clear stripes as found in the
339 deep basin representing the steadily formed oceanic crust (Fig. 9a). Such long-wavelength
340 magnetic anomalies can also be recognized alongside other slope regions of the SCS (Fig. 9a).
341 Here, the buried layer (velocity of 3.8 km/s) overlying the basement may represent volcanic
342 extrusions and contribute partly to the magnetic anomaly. In addition, the horizontally overlying
343 strata indicate that these magmatic activities occurred earlier (Fig. 9c). A similar magnetic
344 anomaly has been observed along the OCT of the Central and North Atlantic margins,
345 representing pre-spreading magmatic intrusions or underplating (Nirrengarten et al., 2017).
346 However, normal crustal velocities (5.0-7.0 km/s) and a reflective Moho in our model exclude
347 both underplated melting and exhumed mantle as an explanation for these anomalies. More

348 likely, the faults at the rim of blocks, as well as the igneous intrusion suggest a hyper-thinned
349 continental crust in this region.

350 We also compiled the crustal structures along the slope regions with high magnetic
351 anomaly in the NW margin and the oceanic basins from published velocity models (Fig. 9b)
352 (Huang et al., 2011; Wu et al., 2011; Zhang et al., 2016; Zhao et al., 2018). The structures share
353 common characteristics including a narrow high velocity band and a high velocity gradient of the
354 upper crust similar to the global characteristics of the OCT (Christensen and Mooney, 1995).
355 Variation of the crustal thicknesses (6-9 km) can be explained by extents of magmatic additions
356 or influences from pre-rifting structures. In contrast, the normal oceanic crust is relatively thin,
357 about 5 to 8 km. The seismic velocity and gradient of layer 2 in the spreading ridge (C5e-C5c)
358 decreased rapidly compared to that near the OCT region (C12-C11) (Fig.9b), reflecting a greater
359 degree of fracturing and less compaction of the cracks (White et al., 1992). At the same time,
360 there are similar velocity differences between the OCT and the NW Sub-basin with the oldest
361 oceanic crust (Fig. 9a, b). The narrow OCT (~50 km), as well as the volcanic intrusions and
362 extrusions suggest a prominent magmatism at late-stage rifting, which may lead to a rapid onset
363 of the embryonic oceanic crust mixed with the highly fractured continental crust (Fig. 10c-d).
364 The results are consistent with the IODP drilling that revealed a narrow and fast rift-to-drift
365 transition with abundant MORB-type melts along the margin of the NW Sub-basin (Larsen et al.,
366 2018).



367

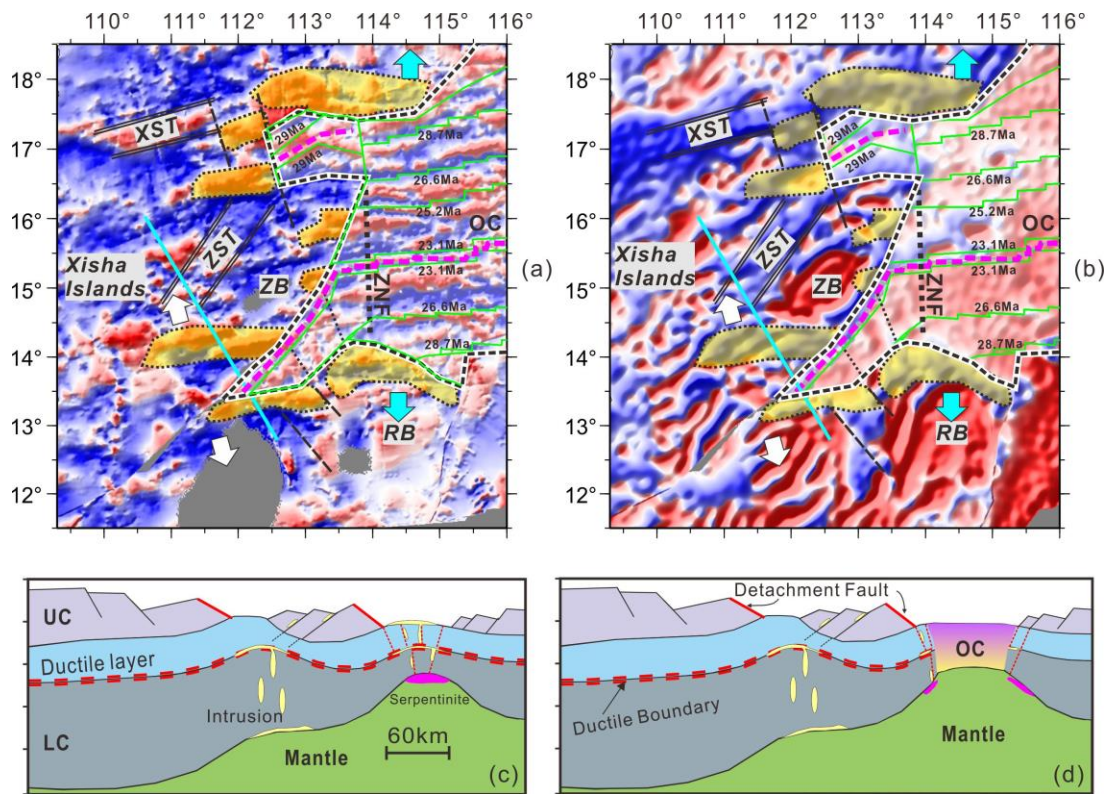
368 Fig. 9 (a) Magnetic anomaly map of the SCS. Dashed yellow lines denote OBS profiles along the
 369 NW margin, while solid blue lines denote the ones at the spreading ridge. The solid purple line
 370 denotes a segment of the OBS2006-1 in the NW Sub-basin. Green lines enclose high magnetic
 371 anomalies near the slopes. Yellow stars are IODP drillings during the 367/368 cruises. NW -
 372 Northwestern Sub-basin; East - Eastern Sub-basin; SW - Southwestern Sub-basin; RB - Reed
 373 Bank; XST – Xisha Trough; ZB – Zhongsha Bank; ZST – Zhongsha Trough; ZH - Zhenghe
 374 Massif; ZSNB – Zhongshanan Basin. (b) Compilation of the velocity structures in the SCS. The
 375 dashed line represents the averaged velocity-depth profile in the Zhongshanan basin. OC –
 376 Oceanic crust. (c) A segment of the reflection seismic profile along the OBS2013-1, which is
 377 denoted by the bold solid yellow line in Fig.9a. The yellow dotted lines denote the sedimentary
 378 boundaries, and the transparent shaded area denotes the buried volcanic extrusions.

379 5.3 Origin of the low-velocity upper mantle and the high magnetic anomaly

380 The obvious low-velocity structure (~ 7.7 km/s; Fig. 5b-c) extending more than 3 km below
381 the Moho in the Zhongjiannan Basin can be interpreted as an indicator of serpentinization in the
382 upper mantle (Miller and Christensen, 1997) or the presence of partial melting (Henry et al.,
383 1990). The ~ 3 km thick molten material with velocity of ~ 7.7 km/s would require a Moho
384 temperature greater than 1000 °C (White and Mckenzie, 1989). However, the heat flow value
385 measured here is about 60 mW/m² (Shi et al., 2002), which roughly means that the temperature
386 below the crust is less than 500 °C, not high enough to cause present-day melting. Since the
387 crust is only ~ 6 km thick, serpentinization could be originating from penetration of water into the
388 upper mantle along the normal faults bordering the blocks (Fig. 10c) (Dean et al., 2000). In this
389 scenario, seismic velocity of ~ 7.7 km/s corresponds to about 13% of the partial serpentinization
390 of the upper mantle (Mechie et al., 1994). A similar serpentinized mantle has been proposed to
391 exist (7.6 km/s in velocity and ~ 3 km in thickness) beneath the fossil spreading ridge in the
392 Southwest Sub-basin (OBS-Zhang; Fig. 1b) (Zhang et al., 2016). There, an extremely low heat
393 flow < 50 mW/m² was measured (He et al., 2001) and was considered to be related to the
394 Zhongnan Fracture Zone (the ZNF in Fig. 1b). In any case, the limited extend of serpentinized
395 mantle may indicate a short-term fault activity (Bayrakci et al., 2016) or oblique extension
396 (White et al., 1992). This agrees again with the narrow OCT in the study region due to the rapid
397 onset of the oceanic crust accretion.

398 Spectral analysis on the magnetic field in the SCS indicates that deep magnetic layers at the
399 lower crust or upper mantle contribute to both the SCMA and anomalies near the OCT (Li and
400 Song, 2012). The mantle serpentinization of $\sim 13\%$ beneath the Zhongshanan Basin, if it exists,
401 should not be the dominant source of the high magnetic anomaly in this area, as very partially
402 serpentinized upper mantle contributes only little to the magnetic anomaly (Fujii et al., 2016).

403 The long-wavelength magnetic anomalies were frequently observed over cratons and forearcs
 404 and were considered to be caused by magnetic uppermost mantle (Ferre et al., 2014). Forward
 405 modeling of the magnetic anomalies from xenoliths show that high magnetization of the upper
 406 mantle usually corresponds to low geothermal settings (Friedman et al., 2014). Normally, rift
 407 valleys such as the Zhongsha Trough might be too hot to form strong mantle magnetism, which
 408 is verified by the magnetic data in the northwestern margin (Fig.9a). However, the heat flow
 409 values are commonly low along the Zhongjiannan Basin, which may be related to the highly
 410 fractured crust. The deep mantle magma accompanying the formation of the embryonic oceanic
 411 crust could have provided material source for the mantle magnetite.



412
 413 Fig. 10 Maps of the magnetic (a) and gravity anomaly (b) of the SCS reconstructed at 22.5 Ma
 414 using rotation poles from the Gplates software (Boyden et al., 2011). Yellow areas mask the high
 415 magnetic anomaly representing the OCT along the slopes. Green lines are identified magnetic

416 anomalies, representing mature oceanic crust. The blue and white arrows represent the early and
417 late stages of the seafloor spreading (Briais et al., 1993), respectively. Thin dashed lines
418 represent the possible transform faults identified based on the gravity and magnetic anomalies.
419 Bold dashed lines denote the reconstructed COB. (c, d): Schematic models for the evolution of
420 the continental margin before (c) and after (d) the seafloor spreading between the Zhongsha
421 Bank (ZB) and the Reed Bank (RB). The location is shown by the blue lines in Fig. 10a and Fig.
422 10b. UC - upper crust; LC - lower crust; OC - Oceanic crust.

423 **6 Conclusions**

424 Precisely reflection and wide-angle seismic modeling revealed the crustal structures in the
425 NW margin of the SCS. The conclusions are as following: 1) Crustal deformation was controlled
426 by detachment faults that sole out into a ductile layer at depths of ~7 km below the basement. A
427 sharp velocity boundary exists between this ductile layer and the lower crust in the Zhongsha
428 Trough. 2) The brittle upper crust has been detached along a ~20 km wide zone in the Zhongsha
429 Trough, accompanied by thickened lower crust due to magmatic additions. 3) A highly thinned
430 continental crust (~6 km thick) in the Zhongshanan Basin represents the OCT where high
431 magnetic anomaly is related to magmatic addition and upper mantle magnetism. Below the crust,
432 the upper mantle was likely to be partially serpentinized due to short-term fault activity shortly
433 before the oceanic spreading. 4) Prominent magmatism at late-stage rifting penetrated the OCT
434 and may lead to a rapid onset of the embryonic oceanic crust.

435 **Acknowledgments**

436 The NSFC Open Research Cruise (NORC2013-08), funded by the Shiptime Sharing Project of
437 NSFC, has supported the data acquisition of this work. This cruise was conducted onboard R/V
438 “Shiyan 2” by the scientific team and the crew. This study was supported by National Key R&D

439 Program of China [grant number: 2018YFC0309800] and National Natural Science Foundation
440 of China [grant numbers: 41676045, 41674092 and 41306046]. The GMT software (Wessel and
441 Smith, 1995) and Seismic Unix software package (Stockwell, 1999) were used to plot the figures.
442 We thank Stephane Operto for providing codes packages of filtering and deconvolution of OBS
443 data. We also thank Dieter Franke for his constructive comments on the discussion. Datasets for
444 this research are available at the link <http://doi.org/10.5281/zenodo.3677587>.

445 **References**

- 446 1. Ao, W., Zhao, M.H., Qiu, X.L., Ruan, A.G., Li, J.B., 2012. Crustal structure of the
447 Northwest Sub-Basin of the South China Sea and its tectonic implication. *Earth Science -
448 Journal of China University of Geosciences (in Chinese)* 37, 779-790.
- 449 2. Bayrakci, G., Minshull, T.A., Sawyer, D.S., Reston, T.J., Klaeschen, D., Papenberg, C.,
450 Ranero, C., Bull, J.M., Davy, R.G., Shillington, D.J., Perez-Gussinye, M., Morgan, J.K.,
451 2016. Fault-controlled hydration of the upper mantle during continental rifting. *Nat Geosci* 9,
452 384-388.
- 453 3. Boyden, J.A., Müller, R.D., Gurnis, M., Torsvik, T.H., Clark, J.A., Turner, M., Ivey-Law, H.,
454 Watson, R.J., Cannon, J.S., 2011. Next-generation plate-tectonic reconstructions using
455 GPlates. *Geoinformatics Cyber infrastructure for the Solid Earth Sciences*, 95-114.
- 456 4. Briais, A., Partriat, P., Tapponnier, P., 1993. Updated interpretation of magnetic anomalies
457 and seafloor spreading in the South China Sea: Implications for the Tertiary Tectonics of
458 Southeast Asia. *J Geophys Res* 98, 6299-6328.
- 459 5. Brune, S., Heine, C., Perez-Gussinye, M., Sobolev, S.V., 2014. Rift migration explains
460 continental margin asymmetry and crustal hyper-extension. *Nat Commun* 5, doi: 10.1038/
461 ncomms5014.

- 462 6. Christensen, N.I., Mooney, W.D., 1995. Seismic Velocity Structure and Composition of the
463 Continental-Crust - a Global View. *J Geophys Res-Sol Ea* 100, 9761-9788.
- 464 7. Dean, S.M., Minshull, T.A., Whitmarsh, R.B., Louden, K.E., 2000. Deep structure of the
465 ocean-continent transition in the southern Iberia Abyssal Plain from seismic refraction
466 profiles: The IAM-9 transect at 40 degrees 20 ' N. *J Geophys Res-Sol Ea* 105, 5859-5885.
- 467 8. Ding, W.W., Li, J.B., 2016. Propagated rifting in the Southwest Sub-basin, South China Sea:
468 Insights from analogue modelling. *J Geodyn*, 100, 71-86.
- 469 9. Ferre, E.C., Friedman, S.A., Martin-Hernandez, F., Feinberg, J.M., Till, J.L., Ionov, D.A.,
470 Conder, J.Z., 2014. Eight good reasons why the uppermost mantle could be magnetic.
471 *Tectonophysics* 624, 3-14.
- 472 10. Franke, D., Savva, D., Pubellier, M., Steuer, S., Mouly, B., Auxietre, J.L., Meresse, F.,
473 Chamot-Rooke, N., 2014. The final rifting evolution in the South China Sea. *Mar Petrol*
474 *Geol* 58, 704-720.
- 475 11. Friedman, S.A., Feinberg, J.M., Ferre, E.C., Demory, F., Martin-Hernandez, F., Conder, J.A.,
476 Rochette, P., 2014. Craton vs. rift uppermost mantle contributions to magnetic anomalies in
477 the United states interior. *Tectonophysics* 624, 15-23.
- 478 12. Fujii, M., Okino, K., Sato, H., Nakamura, K., Sato, T., Yamazaki, T., 2016. Variation in
479 magnetic properties of serpentinitized peridotites exposed on the Yokoniwa Rise, Central
480 Indian Ridge: Insights into the role of magnetite in serpentinitization. *Geochem Geophys*
481 *Geosy* 17, 5024-5035.
- 482 13. Gao, J.W., Wu, S.G., McIntosh, K., Mi, L.J., Liu, Z., Spence, G., 2016. Crustal structure and
483 extension mode in the northwestern margin of the South China Sea. *Geochem Geophys*
484 *Geosy* 17, 2143-2167.

- 485 14. Hayes, D.E., Nissen, S.S., 2005. The South China Sea margins: Implications for rifting
486 contrasts. *Earth Planet Sc Lett* 237, 601-616.
- 487 15. He, L.J., Wang, K.L., Xiong, L.P., Wang, J.Y., 2001. Heat flow and thermal history of the
488 South China Sea. *Phys Earth Planet In* 126, 211-220.
- 489 16. Henry, W.J., Mechie, J., Maguire, P.K.H., Khan, M.A., Prodehl, C., Keller, G.R., Patel, J.,
490 1990. A Seismic Investigation of the Kenya Rift-Valley. *Geophysical Journal International*
491 100, 107-130.
- 492 17. Huang, H.B., Qiu, X.L., Xu, H.L., Zhao, M.H., Hao, T.Y., Xu, Y., Li, J.B., 2011.
493 Preliminary results of the earthquake observation and the onshore offshore seismic
494 experiments on Xisha Block. *Chinese J. Geophys.* (in Chinese) 54, 3161-3170.
- 495 18. Huang, H.B., Qiu, X.L., Pichot, T., Klingelhoefer., F., Zhao, M.H., Wang, P., Hao, T.Y.,
496 2019. Seismic structure of the northwestern margin of the South China Sea: implication for
497 asymmetric continental extension. *Geophys. J. Int.* 218, 1246-1261.
- 498 19. Huisman, R.S., Beaumont, C., 2014. Rifted continental margins: The case for depth-
499 dependent extension. *Earth Planet Sc Lett* 407, 148-162.
- 500 20. Jian, Z.M., Larsen, H.C., and Alvarez Zarikian, C.A., and the Expedition 368 Scientists,
501 2018. Expedition 368 preliminary report: South China Sea rifted margin: International
502 Ocean Discovery Program. doi: 10.14379/iodp.pr.368.2018
- 503 21. Jin, X.L., 1989. The geosciences research report in South China Sea. *Donghai Mar. Sci.*, (in
504 Chinese) 7, 30-42.
- 505 22. Korenaga, J., Holbrook, W.S., Kent, G.M., Kelemen, P.B., Detrick, R.S., Larsen, H.C.,
506 Hopper, J.R., Dahl-Jensen, T., 2000. Crustal structure of the Southeast Greenland margin

- 507 from joint refraction and reflection seismic tomography. *Journal of Geophysical Research*
508 *Atmospheres* 105, 21591-21614.
- 509 23. Larsen, H.C., Mohn, G., Nirrengarten, M., Sun, Z., Stock, J., Jian, Z., Klaus, A., Alvarez-
510 Zarikian, C.A., Boaga, J., Bowden, S.A., Briais, A., Chen, Y., Cukur, D., Dadd, K., Ding,
511 W., Dorais, M., Ferré, E.C., Ferreira, F., Furusawa, A., Gewecke, A., Hinojosa, J., Höfig,
512 T.W., Hsiung, K.H., Huang, B., Huang, E., Huang, X.L., Jiang, S., Jin, H., Johnson, B.G.,
513 Kurzawski, R.M., Lei, C., Li, B., Li, L., Li, Y., Lin, J., Liu, C., Liu, C., Liu, Z., Luna, A.J.,
514 Lupi, C., McCarthy, A., Ningthoujam, L., Osono, N., Peate, D.W., Persaud, P., Qiu, N.,
515 Robinson, C., Satolli, S., Sauermilch, I., Schindlbeck, J.C., Skinner, S., Straub, S., Su, X., Su,
516 C., Tian, L., van der Zwan, F.M., Wan, S., Wu, H., Xiang, R., Yadav, R., Yi, L., Yu, P.S.,
517 Zhang, C., Zhang, J., Zhang, Y., Zhao, N., Zhong, G., Zhong, L., 2018. Rapid transition
518 from continental breakup to igneous oceanic crust in the South China Sea. *Nat Geosci* 11,
519 782-789.
- 520 24. Lester, R., Van Avendonk, H.J.A., McIntosh, K., Lavier, L., Liu, C.S., Wang, T.K., Wu, F.,
521 2014. Rifting and magmatism in the northeastern South China Sea from wide-angle
522 tomography and seismic reflection imaging. *J Geophys Res-Sol Ea* 119, 2305-2323.
- 523 25. Li, C.F., Song, T.R., 2012. Magnetic recording of the Cenozoic oceanic crustal accretion and
524 evolution of the South China Sea basin. *Chin Sci Bull* 57, 3165-3181.
- 525 26. Li, F.C., Sun, Z., Yang, H.F., 2018. Possible spatial distribution of the Mesozoic volcanic
526 arc in the present-day South China Sea continental margin and its tectonic implications. *J*
527 *Geophys Res-Sol Ea* 123, 6215-6235.

- 528 27. Loureiro, A., Afilhado, A., Matias, L., Moulin, M., Aslanian, D., 2016. Monte Carlo
529 approach to assess the uncertainty of wide-angle layered models: Application to the Santos
530 Basin, Brazil. *Tectonophysics* 683, 286-307.
- 531 28. Ma, Y.B., Wu, S.G., Lv, F.L., Dong, D.D., Sun, Q.L., Lu, Y.T., Gu, M.F., 2011. Seismic
532 characteristics and development of the Xisha carbonate platforms, northern margin of the
533 South China Sea. *J Asian Earth Sci* 40, 770-783.
- 534 29. McIntosh, K., Lavier, L., van Avendonk, H., Lester, R., Eakin, D., Liu, C.S., 2014. Crustal
535 structure and inferred rifting processes in the northeast South China Sea. *Mar Petrol Geol* 58,
536 612-626.
- 537 30. Mechie, J., Fuchs, K., Altherr, R., 1994. The Relationship between Seismic Velocity,
538 Mineral-Composition and Temperature and Pressure in the Upper-Mantle - with an
539 Application to the Kenya Rift and Its Eastern Flank. *Tectonophysics* 236, 453-464.
- 540 31. Miller, D.J., Christensen, N.I., 1997. Seismic velocities of lower crustal and upper mantle
541 rocks from the slow spreading Mid-Atlantic Ridge, south of the Kane transform zone
542 (MARK). *Proceedings of the Ocean Drilling Program Scientific Results* 25, 763-771.
- 543 32. Nirrengarten, M., Manatschal, G., Tugend, J., Kuszniir, N.J., Sauter, D., 2017. Nature and
544 origin of the J-magnetic anomaly offshore Iberia-Newfoundland: implications for plate
545 reconstructions. *Terra Nova* 29, 20-28.
- 546 33. Pichot, T., Delescluse, M., Chamot-Rooke, N., Pubellier, M., Qiu, Y., Meresse, F., 2013.
547 Deep crustal structure of the conjugate margins of the SW South China Sea from wide-angle
548 refraction seismic data. *Mar Petrol Geol* 2013, 1-17.

- 549 34. Qiu, N., Wang, Z.F., Xie, H., Sun, Z.P., Wang, Z.W., Sun, Z., Zhou, D., 2013. Geophysical
550 investigations of crust-scale structural model of the Qiongdongnan Basin, Northern South
551 China Sea. *Marine Geophysical Research* 34, 259-279.
- 552 35. Qiu, X.L., Ye, S.Y., Wu, S.M., Shi, X.B., Zhou, D., Xia, K.Y., Flueh, E.R., 2001. Crustal
553 structure across the Xisha Trough, northwestern South China Sea. *Tectonophysics* 341, 179-
554 193.
- 555 36. Ren, J.Y., Lei, C., 2011. Tectonic stratigraphic framework of Yinggehai-Qiongdongnan
556 Basins and its implication for tectonic province division in South China Sea. *Chinese J.*
557 *Geophys. (in Chinese)* 54, 3303-3314.
- 558 37. Ren, J.Y., Zhang, D.J., Tong, D.J., Huang, A.M., Wang, Y.H., Lei, C., Zuo, Q.M., Zhao,
559 Y.H., He, W.J., Yang, L.L., 2014. Characterizing the nature, evolution and origin of
560 detachment fault in central depression belt, Qiongdongnan Basin of South China Sea:
561 evidence from seismic reflection data. *Acta Oceanol Sin* 33, 118-126.
- 562 38. Shi, X.B., Zhou, D., Qiu, X.L., Zhang, Y.X., 2002. Thermal and rheological structures of the
563 Xisha Trough, South China Sea. *Tectonophysics* 351, 285-300.
- 564 39. Stockwell, J.W., 1999. The CWP/SU: seismic Un*x package, *Comput. Geosci.*, 25, 415-419.
- 565 40. Sun, Z., Stock, J., and Klaus, A., and the Expedition 367 Scientists, 2018. Expedition 367
566 preliminary report: South China Sea rifted margin: International Ocean Discovery Program.
567 doi: 10.14379/iodp.pr.367.2018
- 568 41. Taylor, B., Hayes, D.E., 1983. Origin and history of the South China Sea basin, in: Hayes,
569 D.E. (Ed.), *The tectonic and geologic evolution of Southeast Asia Seas and Islands.*
570 *Geophysical Monograph*, Washington, pp. 23-56.

- 571 42. Thybo, H., Nielsen, C.A., 2009. Magma-compensated crustal thinning in continental rift
572 zones. *Nature* 457, 873-876.
- 573 43. Wan, K.Y., Xia, S.H., Cao, J.H., Sun, J.L., Xu, H.L., 2017. Deep seismic structure of the
574 northeastern South China Sea: Origin of a high-velocity layer in the lower crust. *J Geophys*
575 *Res-Sol Ea* 122, 2831-2858.
- 576 44. Wessel, P., Smith, W.H., 1995. New version of the generic mapping tools, EOS, *Trans. Am.*
577 *Geophys. Un.*, 76, 329.
- 578 45. West, M., Menke, W., Tolstoy, M., Webb, S., Sohn, R., 2001. Magma storage beneath axial
579 volcano on the Juan de Fuca mid-ocean ridge. *Nature*, 413, 833-836.
- 580 46. White, R., McKenzie, D., 1989. Magmatism at Rift Zones - the Generation of Volcanic
581 Continental Margins and Flood Basalts. *J Geophys Res-Solid* 94, 7685-7729.
- 582 47. White, R.S., McKenzie, D., Onions, R.K., 1992. Oceanic Crustal Thickness from Seismic
583 Measurements and Rare-Earth Element Inversions. *J Geophys Res-Sol Ea* 97, 19683-19715.
- 584 48. Wu, Z.L., Li, J.B., Ruan, A.G., Lou, H., Ding, W.W., Niu, X.W., Li, X.B., 2011. Crustal
585 structure of the northwestern sub-basin, South China Sea: Results from a wide-angle seismic
586 experiment. *Sci China Earth Sci (in Chinese)* 41, 1463-1476.
- 587 49. Zelt, C.A., Ellis, R.M., 1988. Practical and efficient ray tracing in two-dimensional media
588 for rapid traveltimes and amplitude forward modeling. *Canadian Journal of Exploration*
589 *Geophysics*. 24, 16-31.
- 590 50. Zelt, C.A., Smith, R.B., 1992. Seismic traveltimes inversion for 2-D crustal velocity structure.
591 *Geophys. J. Int.* 108, 16-34.

- 592 51. Zhang, J., Li, J.B., Ruan, A.G., Wu, Z.L., Yu, Z.T., Niu, X.W., Ding, W.W., 2016. The
593 velocity structure of a fossil spreading centre in the Southwest Sub - basin, South China Sea.
594 *Geol J.* 51, 548-561.
- 595 52. Zhang, M.S., 1991. Quaternary events in Xisha coral reef region. *Quaternary Sciences (in*
596 *Chinese)* 2, 165-177.
- 597 53. Zhao, M.H., He, E.Y., Sibuet, J.C., Sun, L.T., Qiu, X.L., Tan, P.C., Wang, J., 2018. Post-
598 Seafloor Spreading Volcanism in the Central East South China Sea and its Formation
599 Through an Extremely Thin Oceanic Crust. *Geochem Geophys Geosy.* 19, 621-641.
- 600 54. Zhu, J.J., Li, J., Sun, Z.X., Li, S.Z., 2016. Crustal thinning and extension in the northwestern
601 continental margin of the South China Sea. *Geol J.* 51, 286-303.
- 602 55. Zhu, W.L., Xie, X.N., Wang, Z.F., Zhang, D.J., Zhang, C.L., Cao, L.C., Shao, L., 2017. New
603 insights on the origin of the basement of the Xisha Uplift, South China Sea. *Sci China Earth*
604 *Sci.* 60, 2214-2222.

Tectonics

Supporting Information for

Seismic Imaging Of an Intracrustal Deformation In the Northwestern Margin Of the South China Sea: the Role Of a Ductile Layer In the Crust

Haibo Huang^{1,3}, Frauke Klingelhoefer², Xuelin Qiu^{1,3,4}, Yuhan Li^{1,4}, Ping Wang^{1,3}

¹South China Sea Institute of Oceanology, CAS, Guangzhou, P.R. China.

²Department of Marine Geosciences, IFREMER, Plouzané, France.

³Innovation Academy of South China Sea Ecology and Environmental Engineering, Chinese Academy of Sciences, Guangzhou 510301, China

⁴College of Earth and Planetary Sciences, UCAS, Beijing, P.R. China

Contents of this file

Figures S1 to S23

Introduction

The supporting information contains the figures of the forward modeling of each OBS profile. In each figure, the upper panel shows the original seismic profile, the middle panel shows the profile overlain by the calculated traveltimes for the picked phases, and the lower panel shows the velocity model with the seismic ray paths. The phases in each figure are named in the following way: direct water phase (Pw), refracted phases in the sediments (Ps), the crust (Pg) and the upper mantle (Pn), sedimentary reflections (PsP1, PsP2), reflections from the basement (PsP3), reflections from the mid-crustal interface (PcP) and the Moho (PmP).

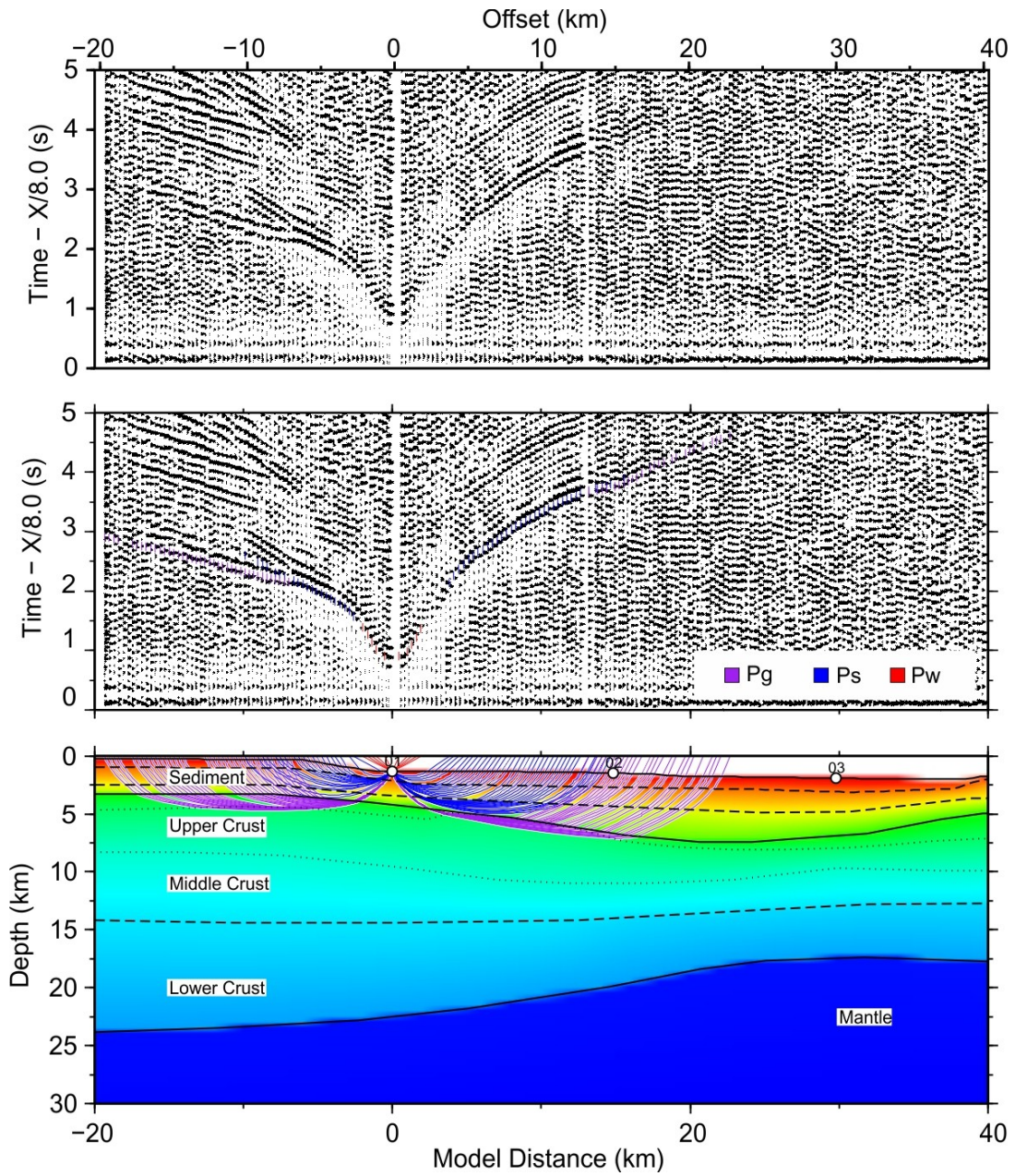


Figure S1. Seismic profile and forward modeling of OBS01

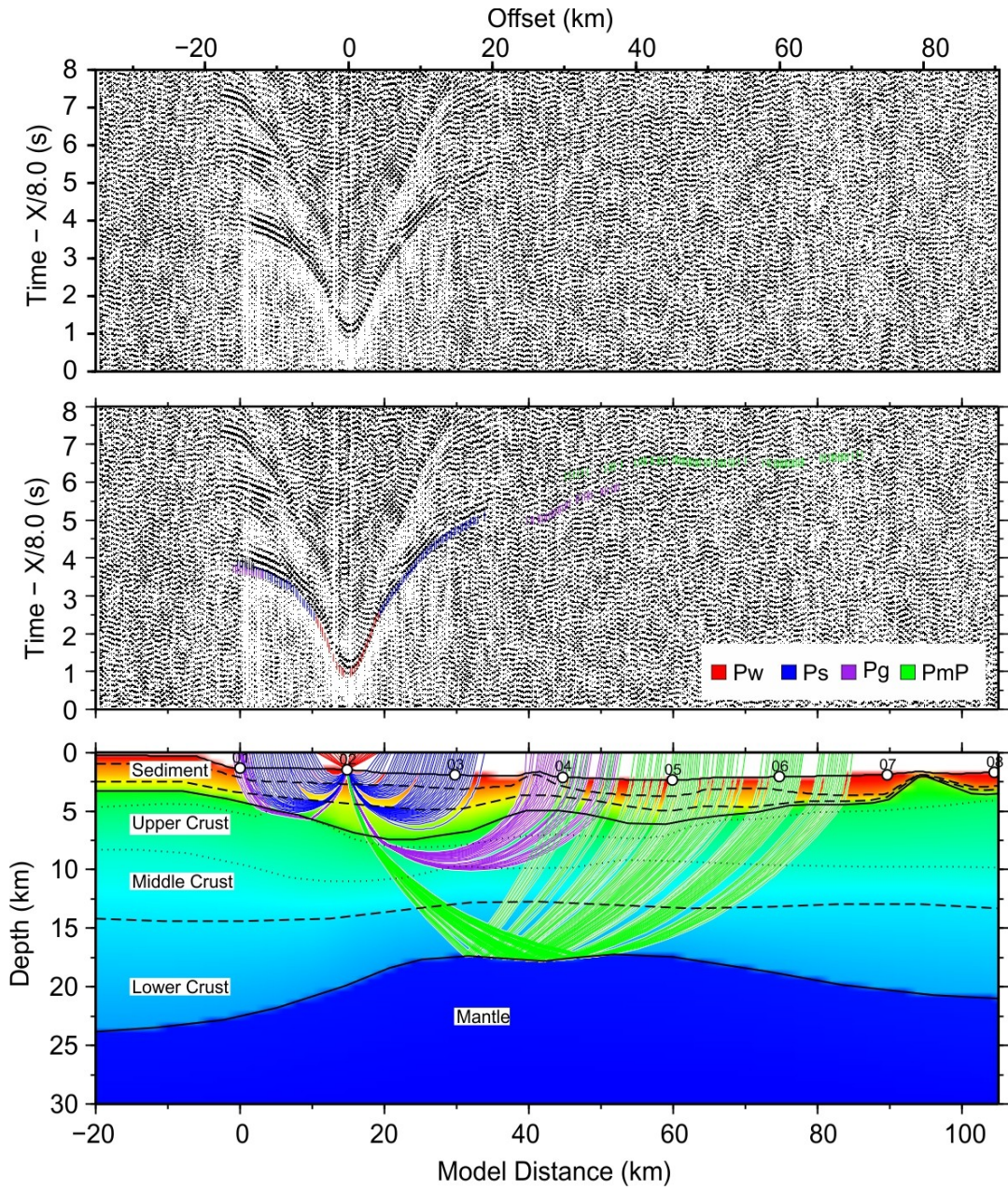


Figure S2. Seismic profile and forward modeling of OBS02

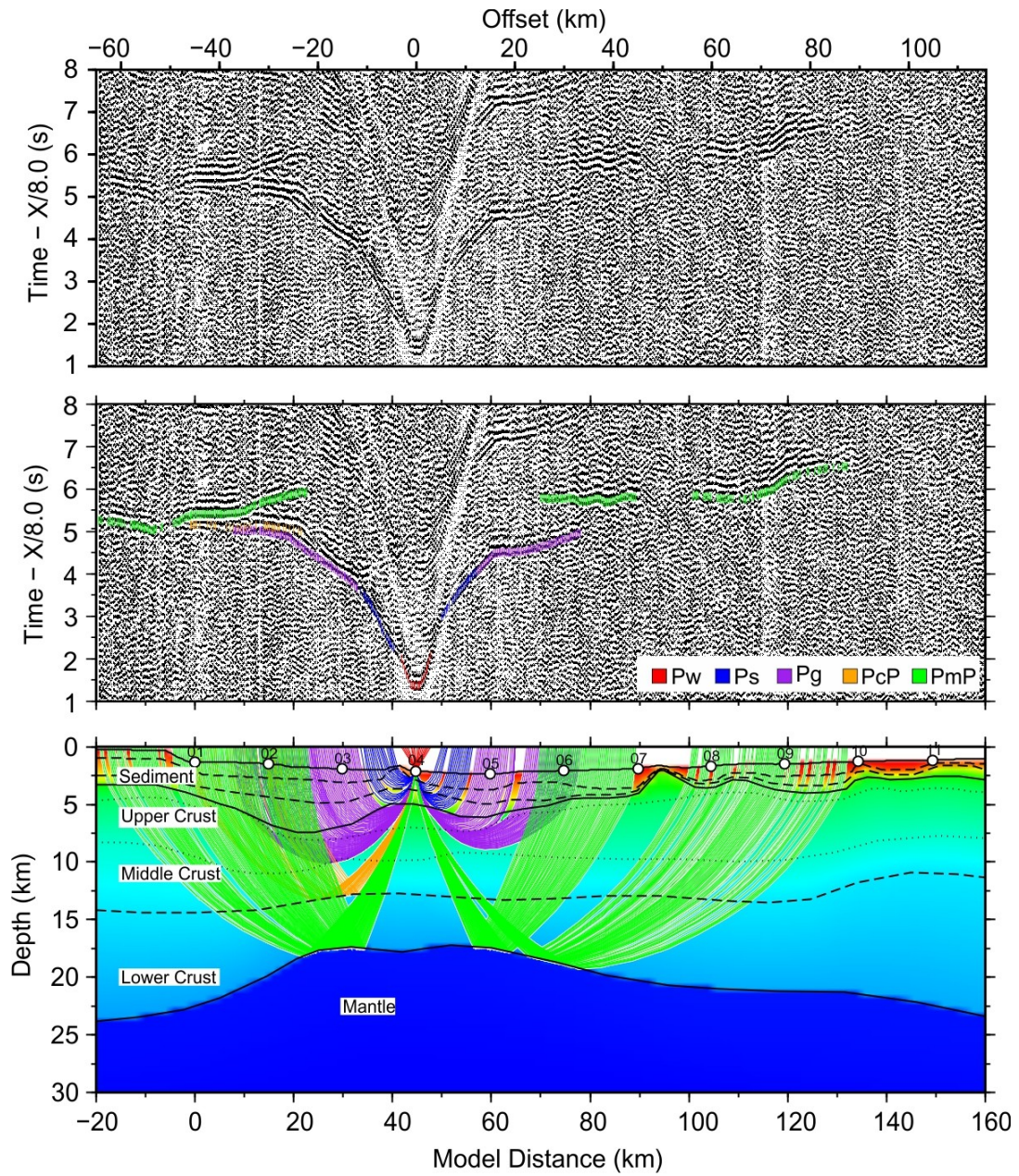


Figure S3. Seismic profile and forward modeling of OBS04

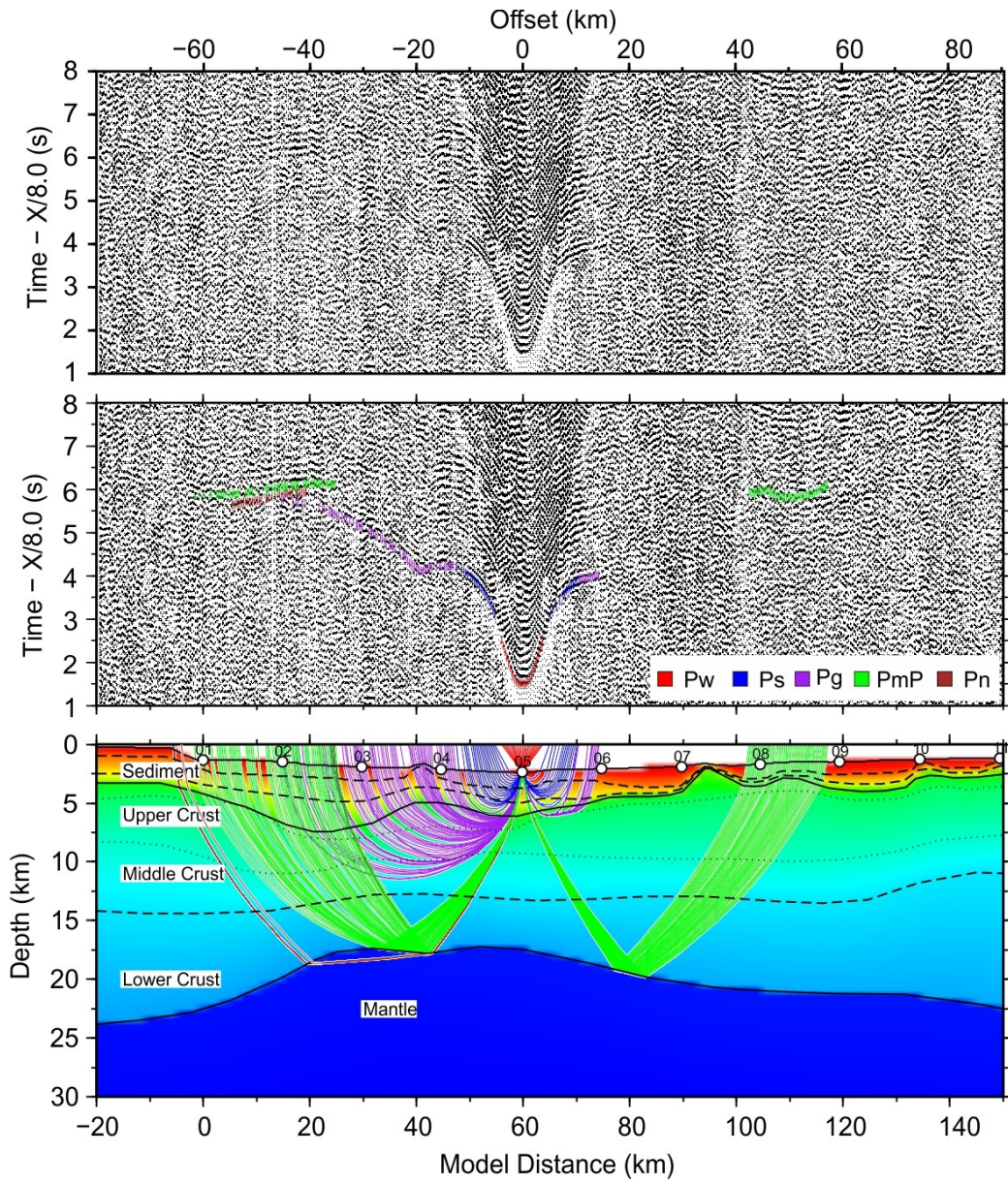


Figure S4. Seismic profile and forward modeling of OBS05

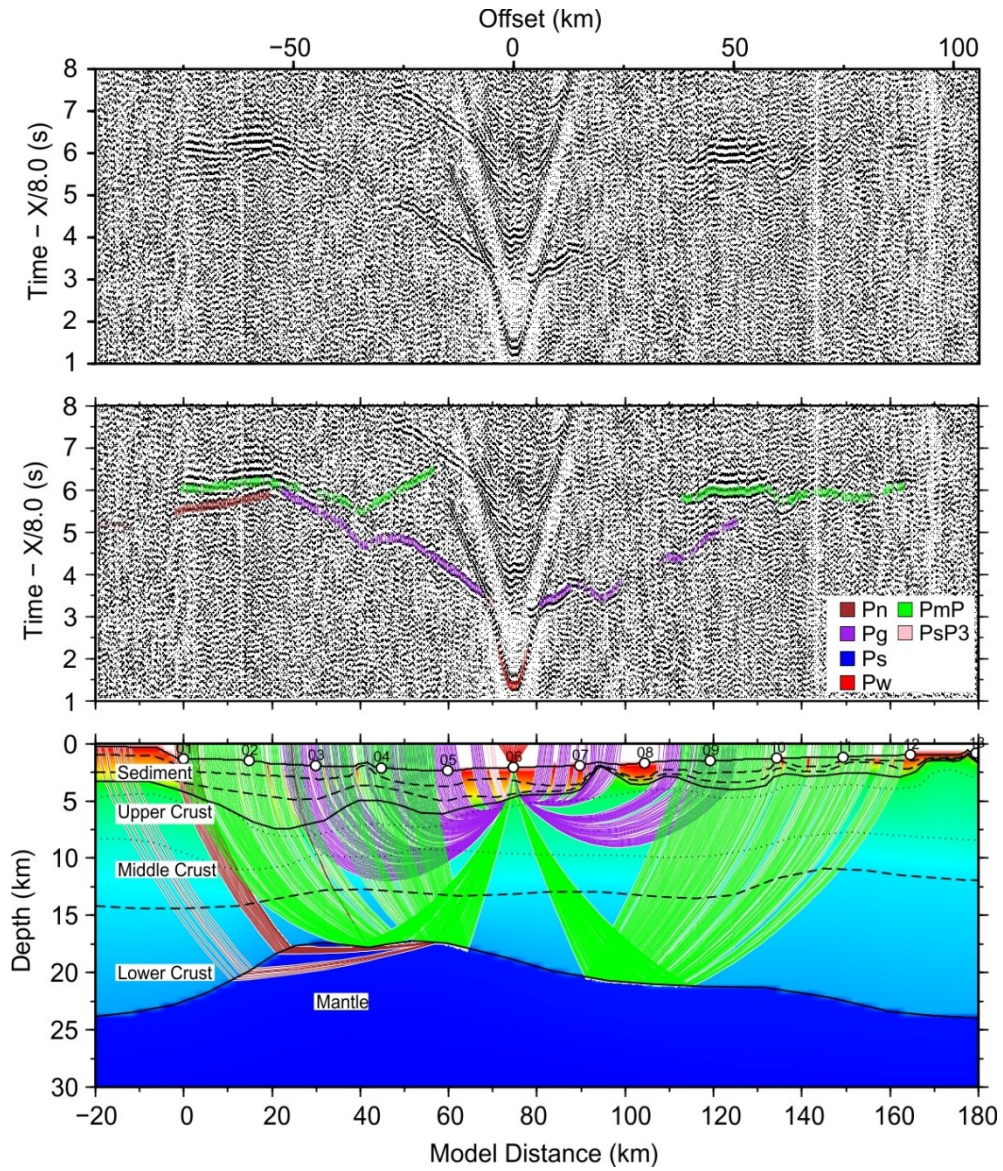


Figure S5. Seismic profile and forward modeling of OBS06

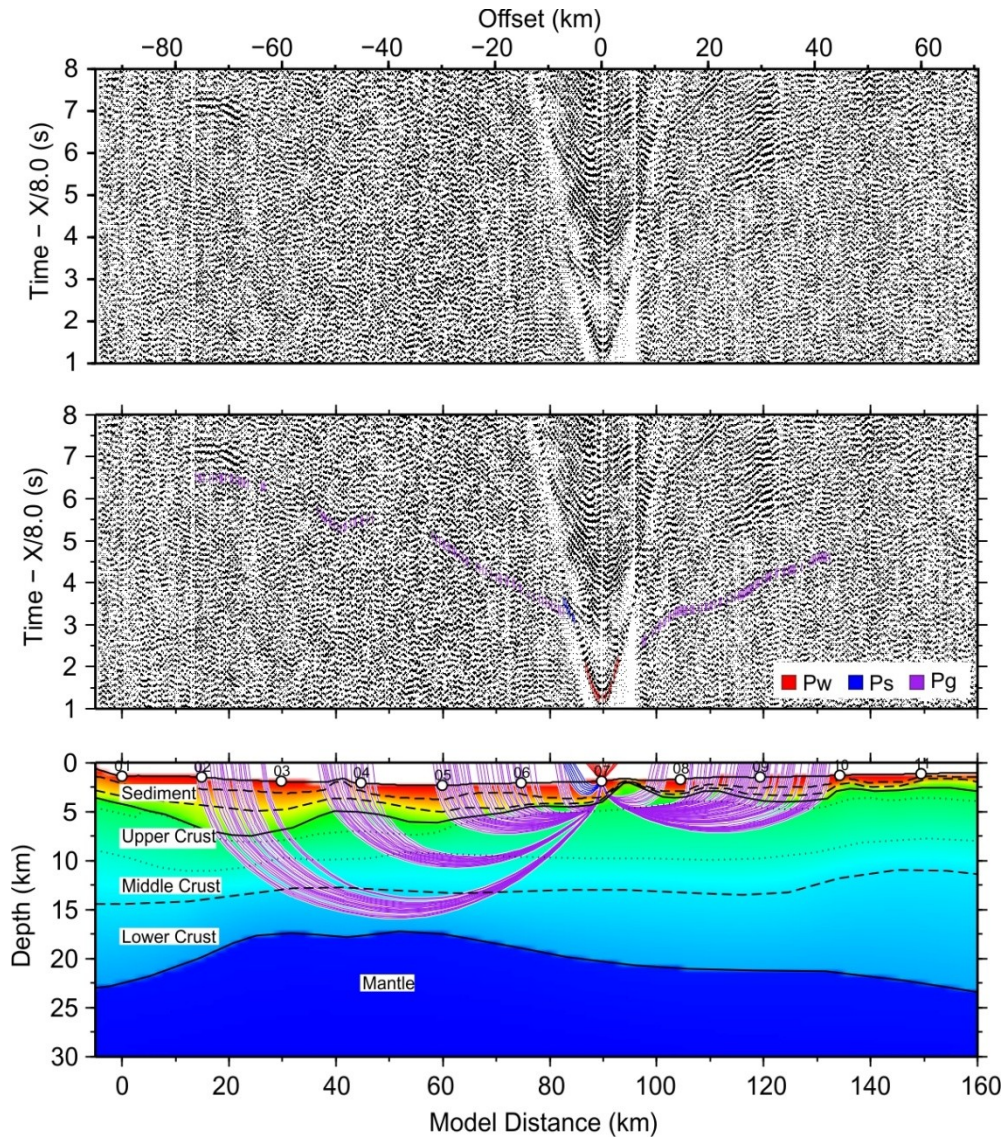


Figure S6. Seismic profile and forward modeling of OBS07

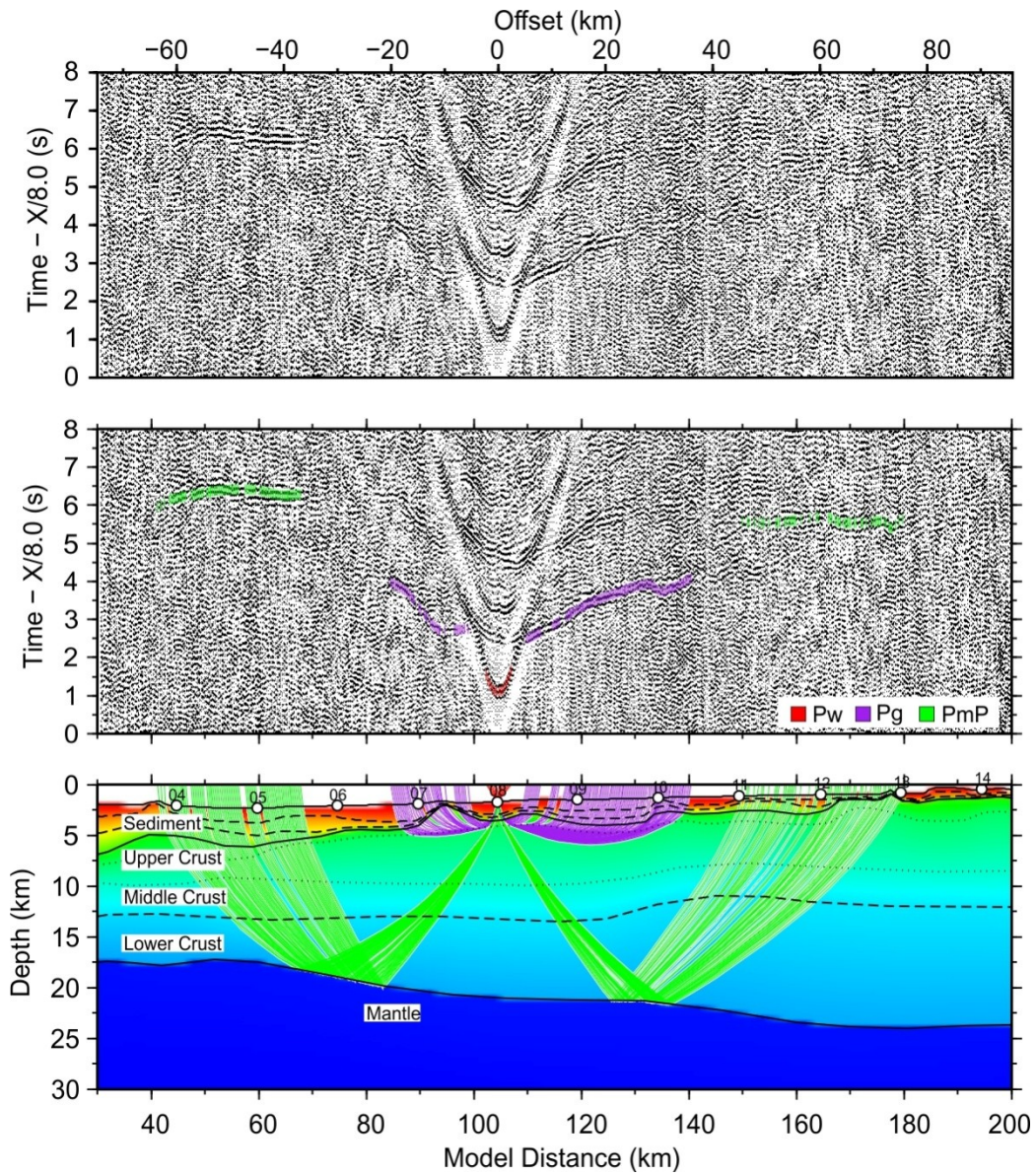


Figure S7. Seismic profile and forward modeling of OBS08

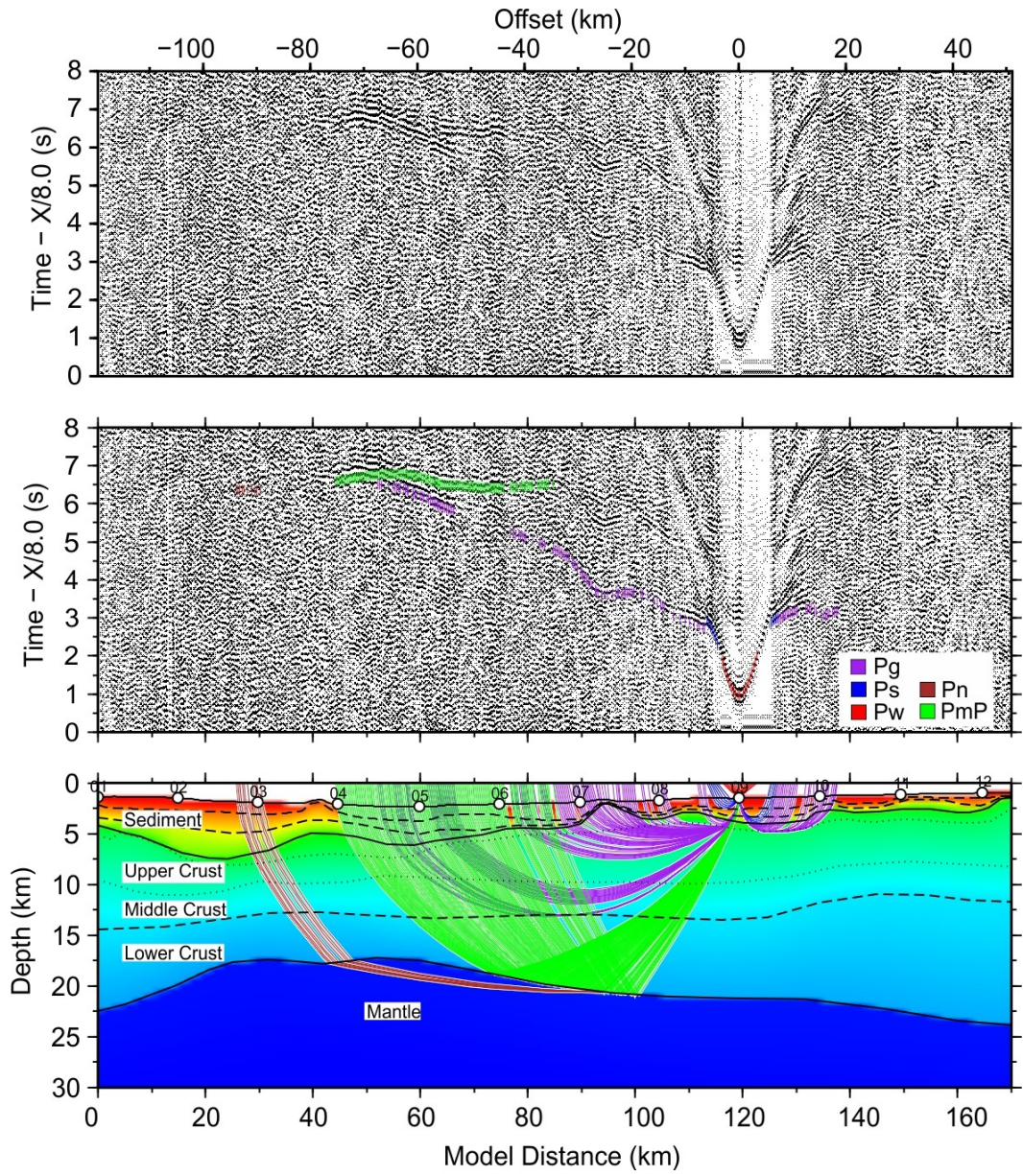


Figure S8. Seismic profile and forward modeling of OBS09

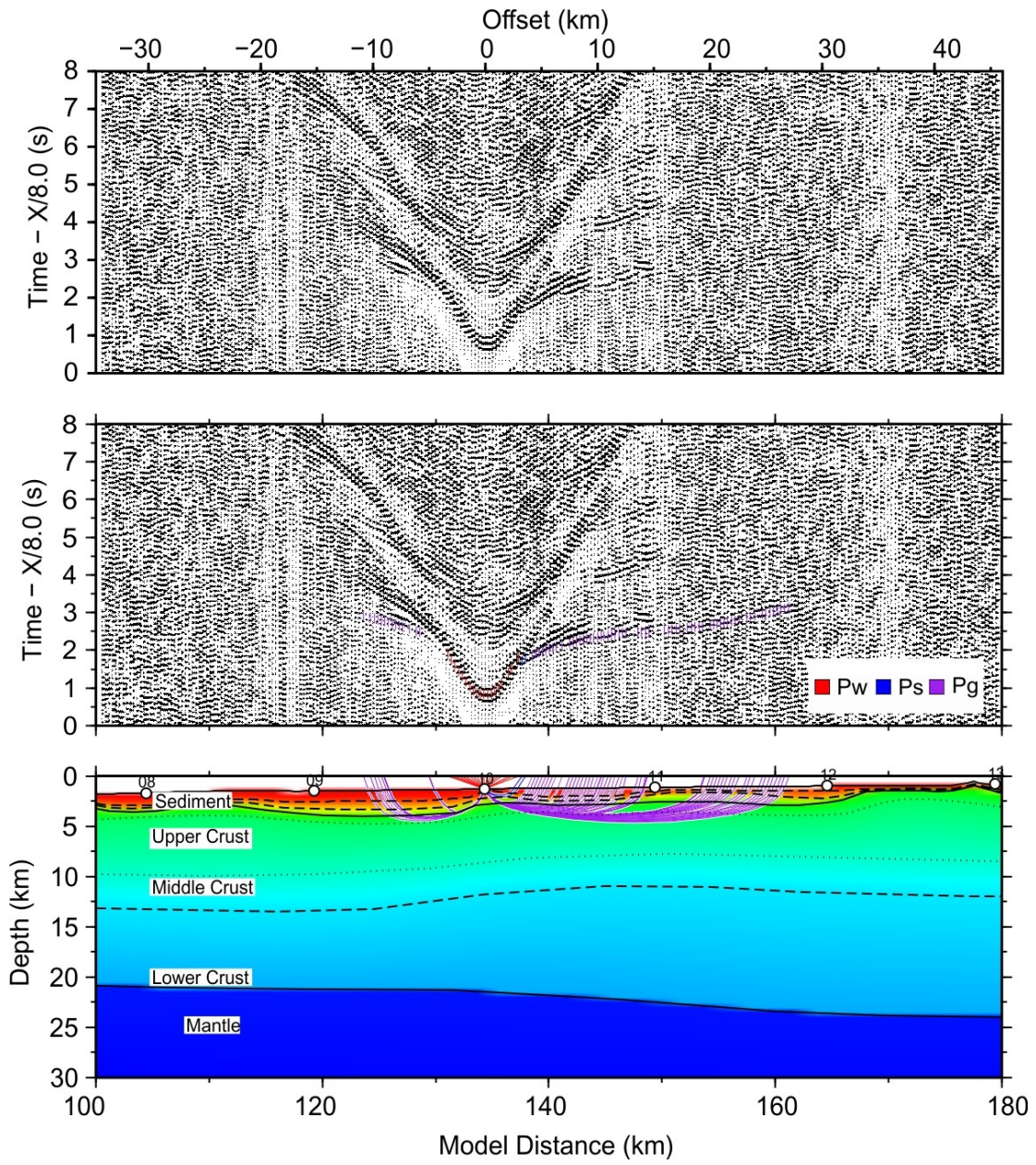


Figure S9. Seismic profile and forward modeling of OBS10

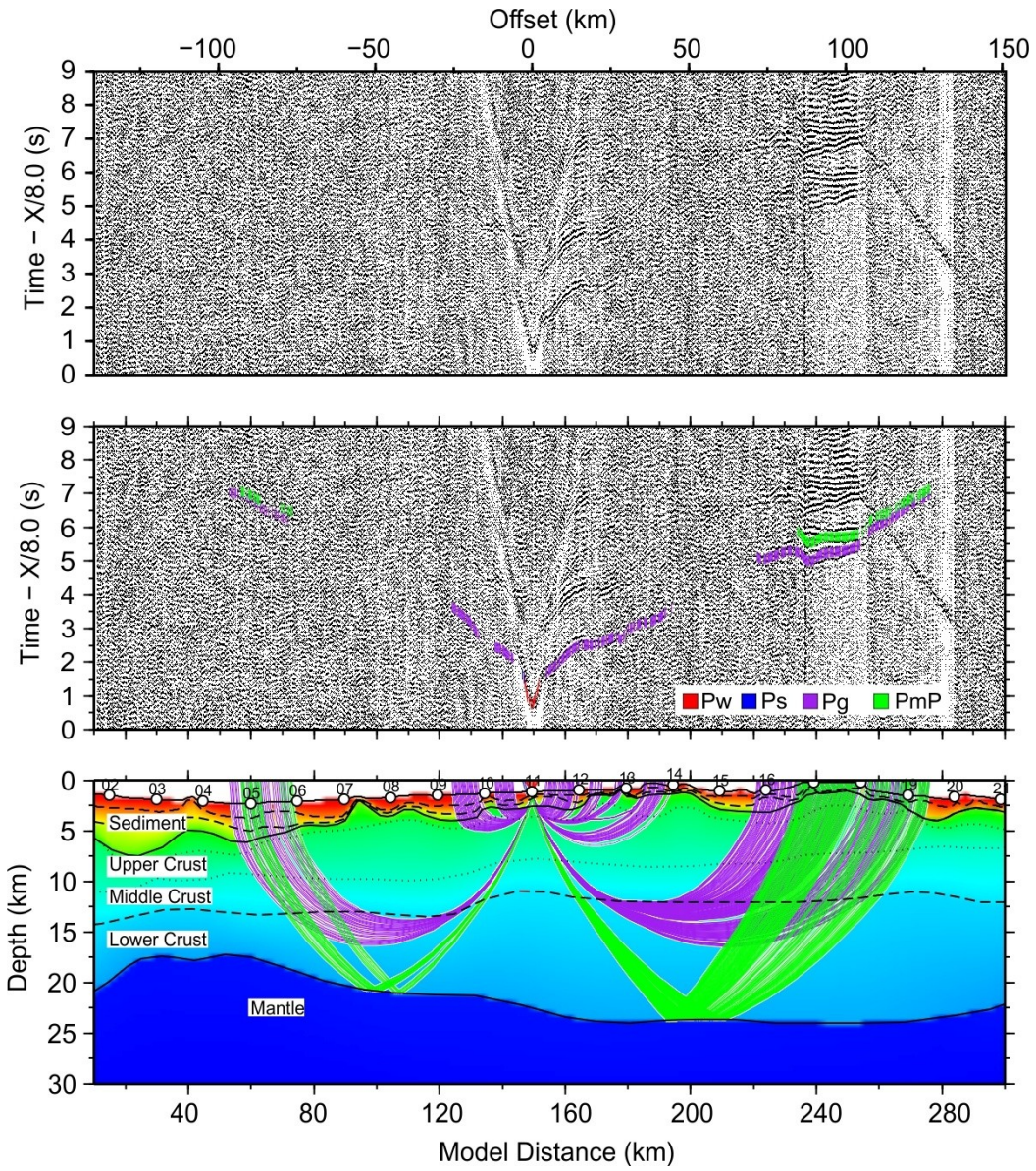


Figure S10. Seismic profile and forward modeling of OBS11

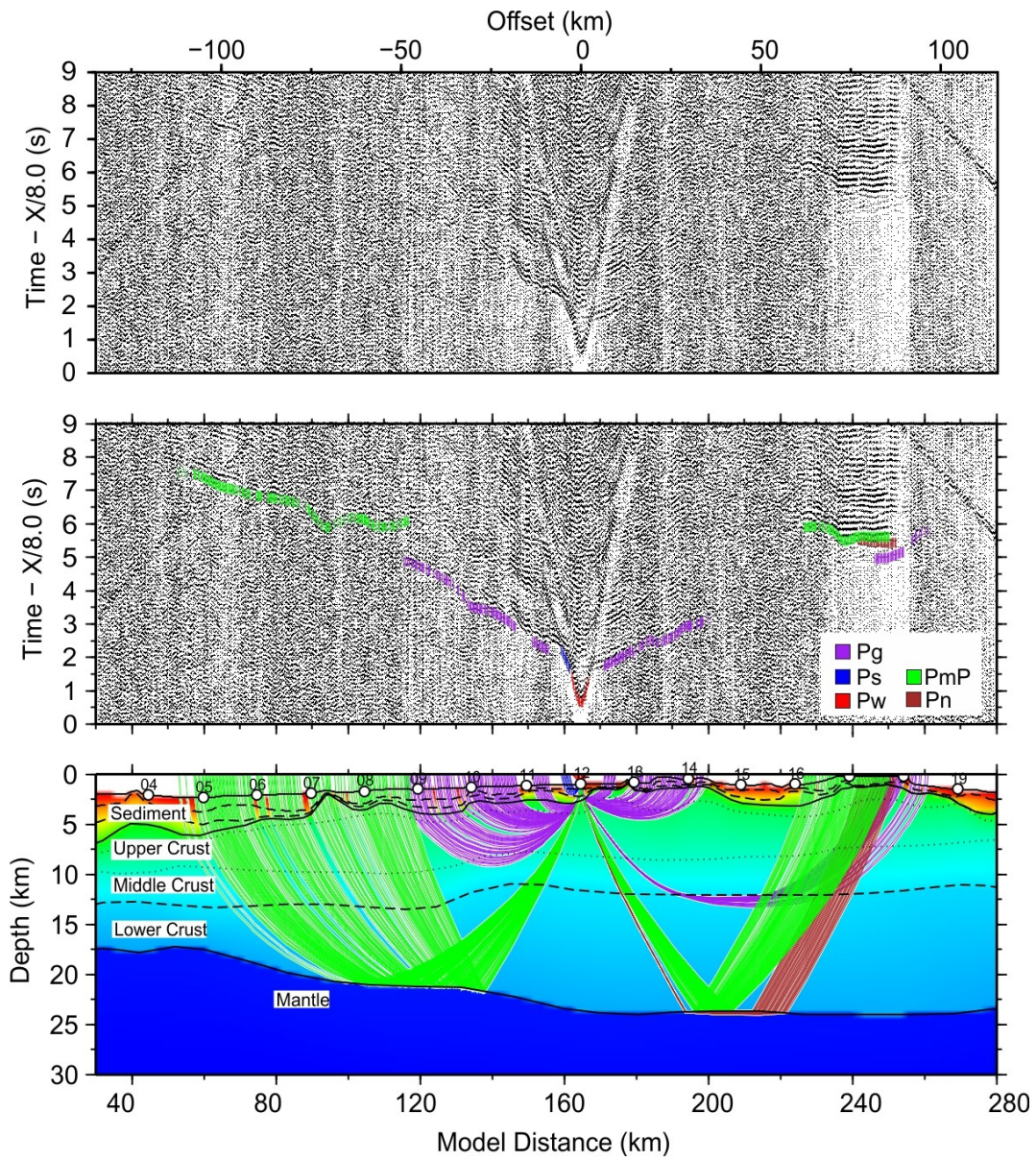


Figure S11. Seismic profile and forward modeling of OBS12

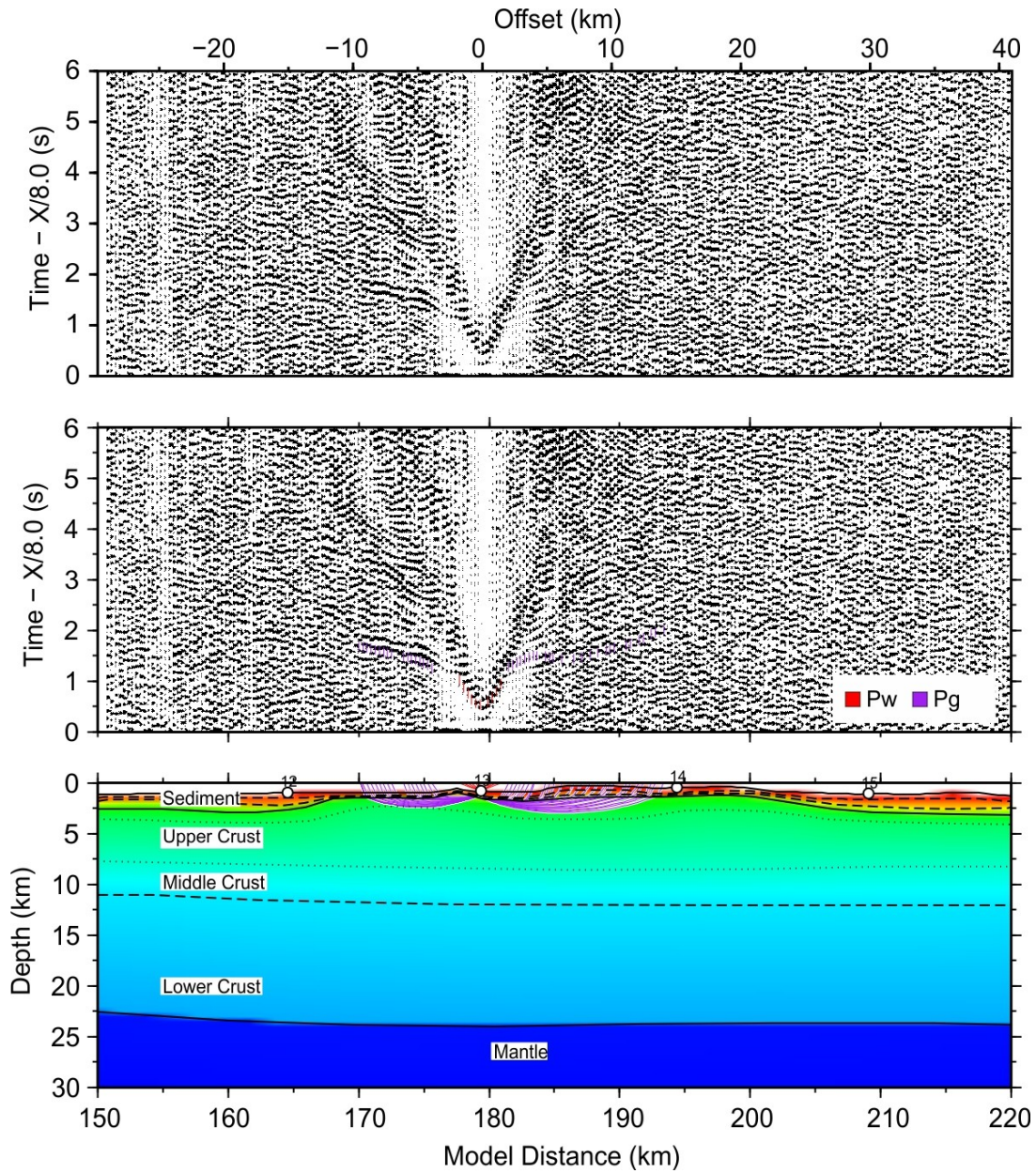


Figure S12. Seismic profile and forward modeling of OBS13

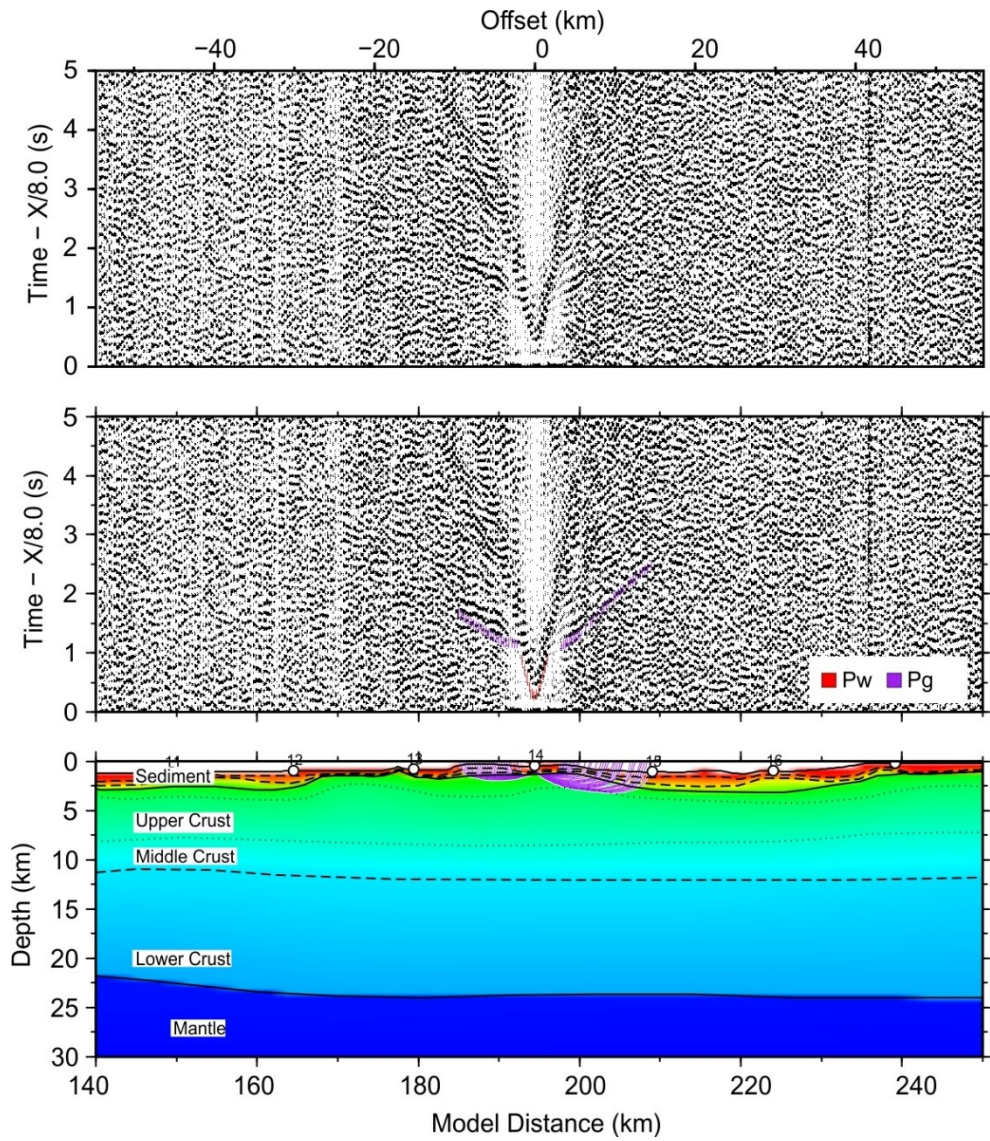


Figure S13. Seismic profile and forward modeling of OBS14

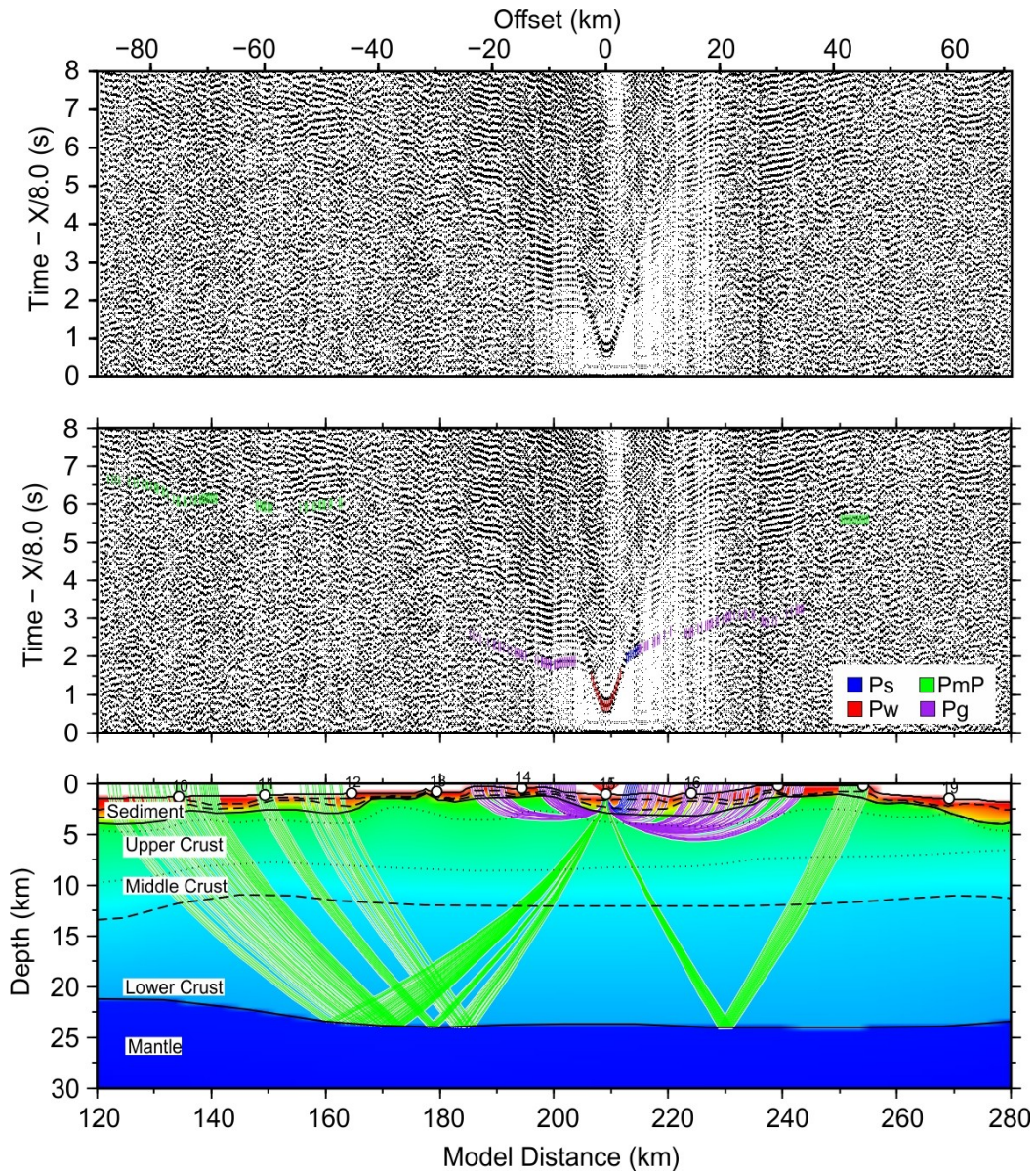


Figure S14. Seismic profile and forward modeling of OBS15

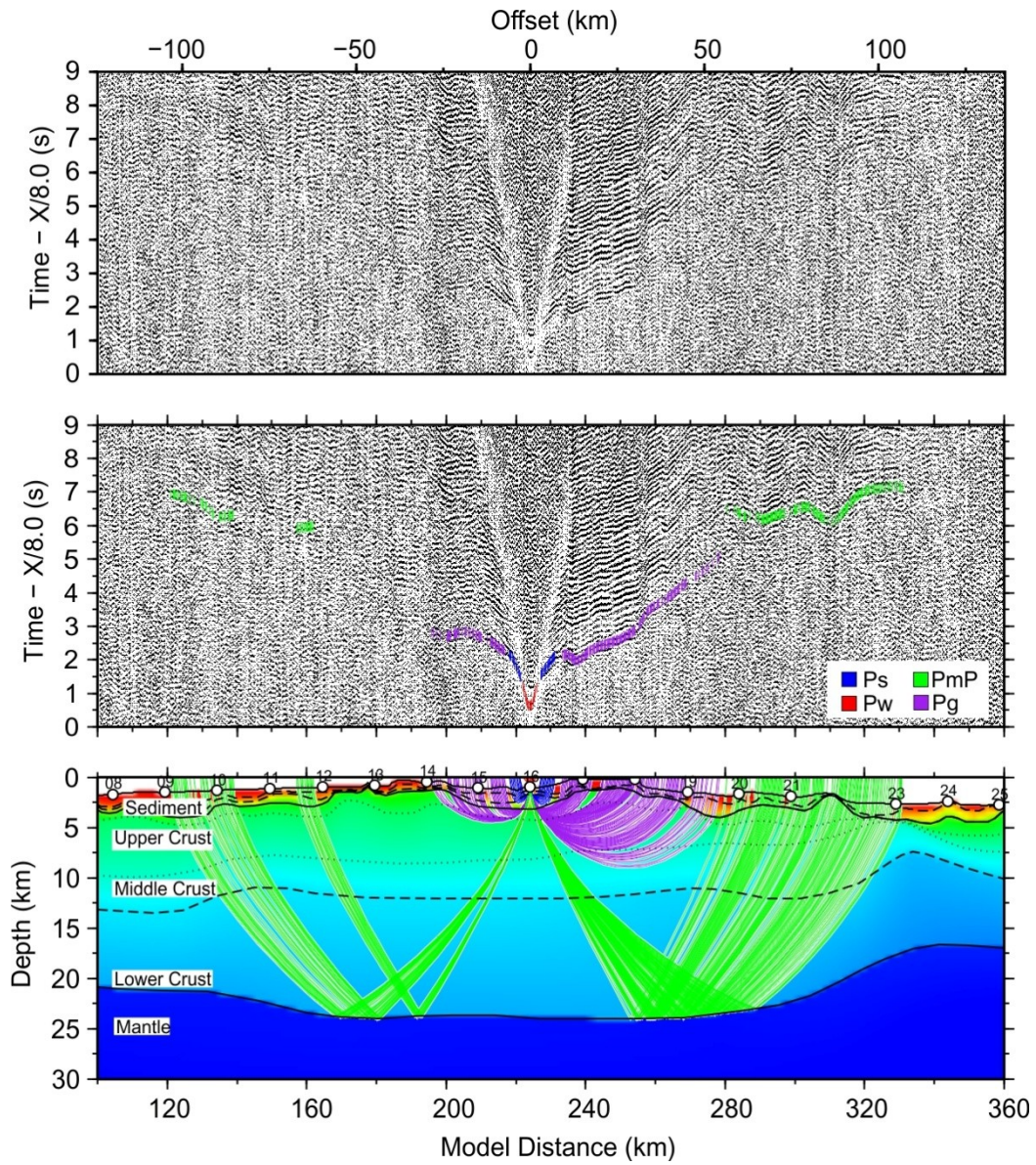


Figure S15. Seismic profile and forward modeling of OBS16

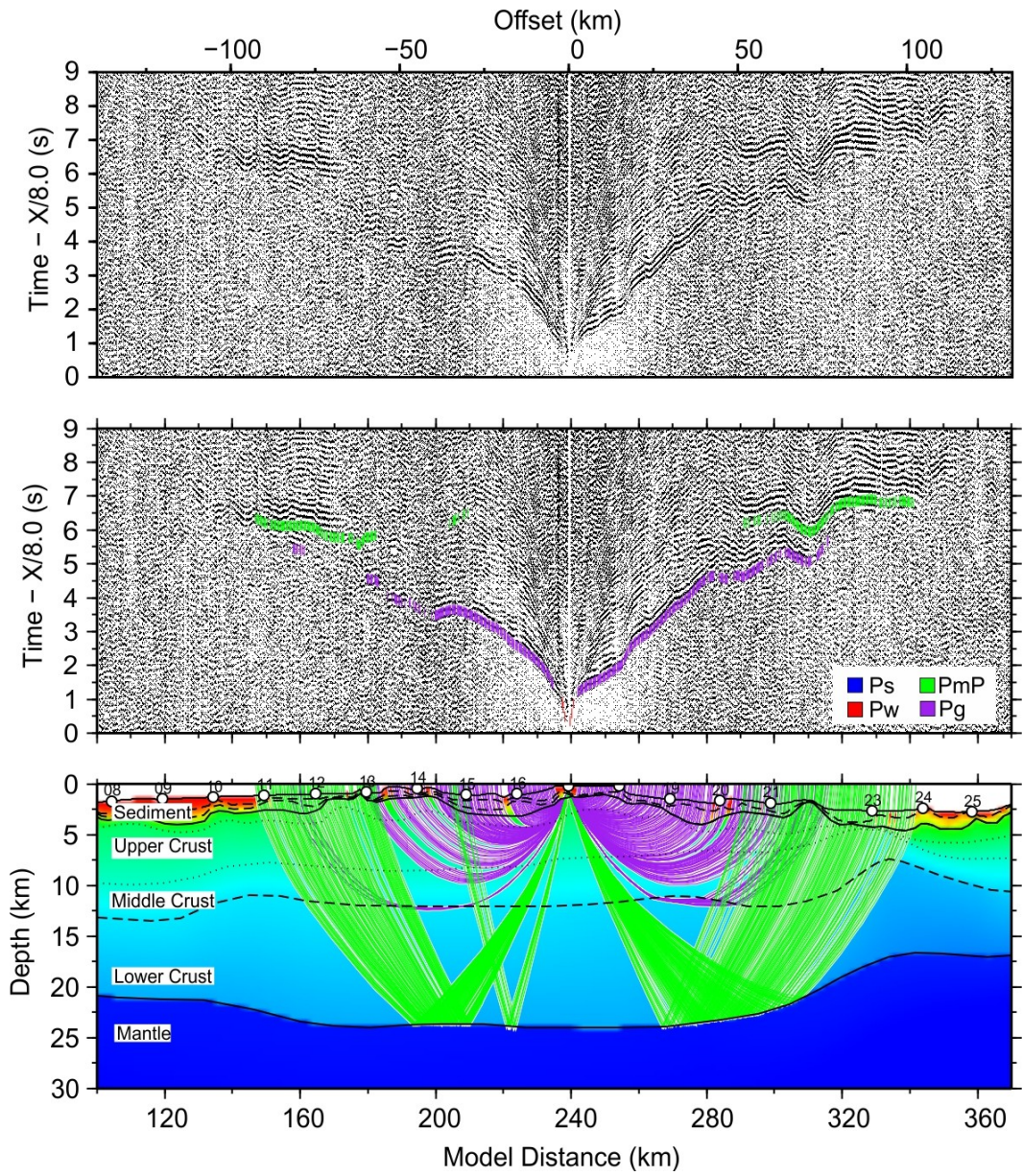


Figure S16. Seismic profile and forward modeling of OBS17

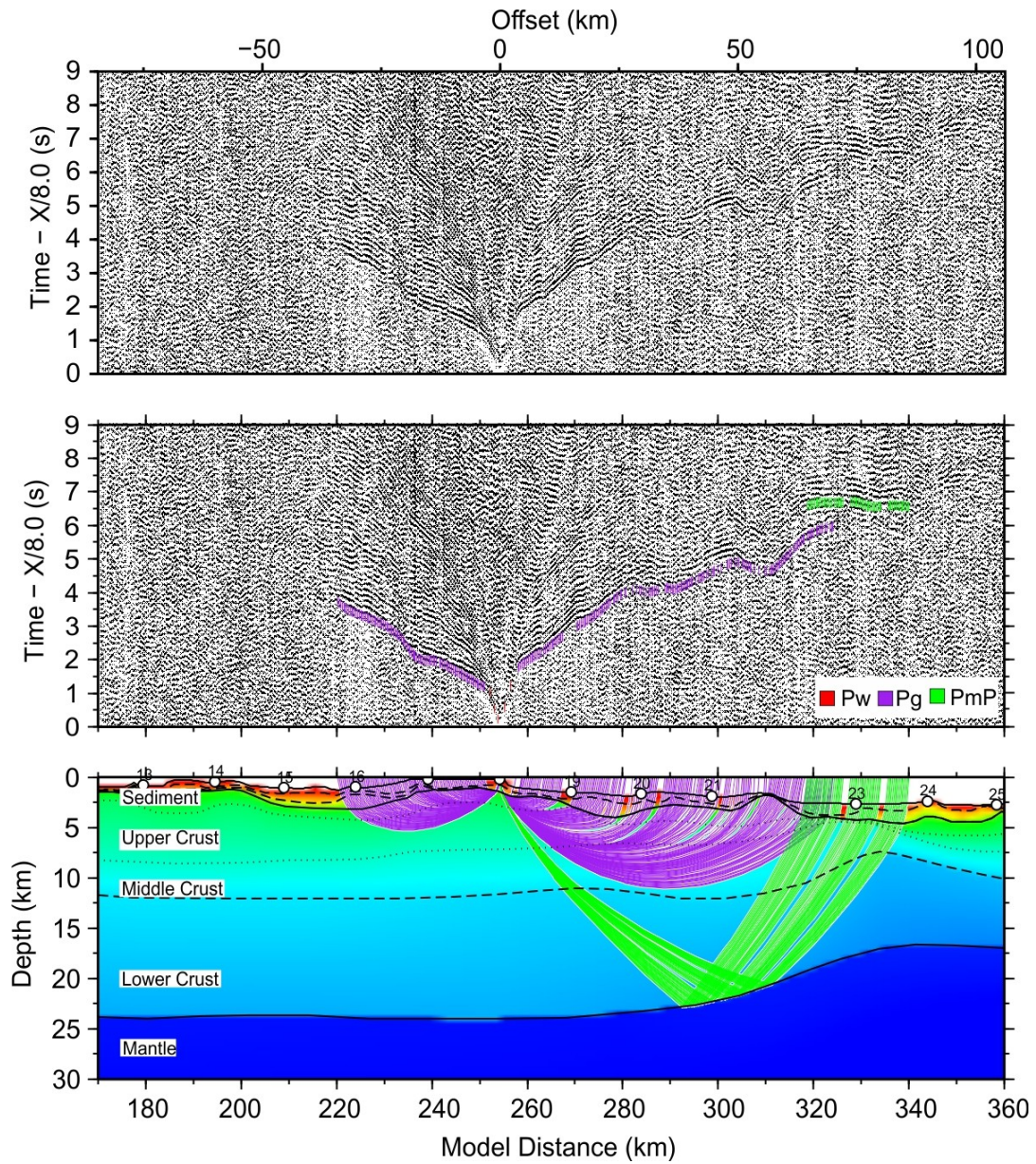


Figure S17. Seismic profile and forward modeling of OBS18

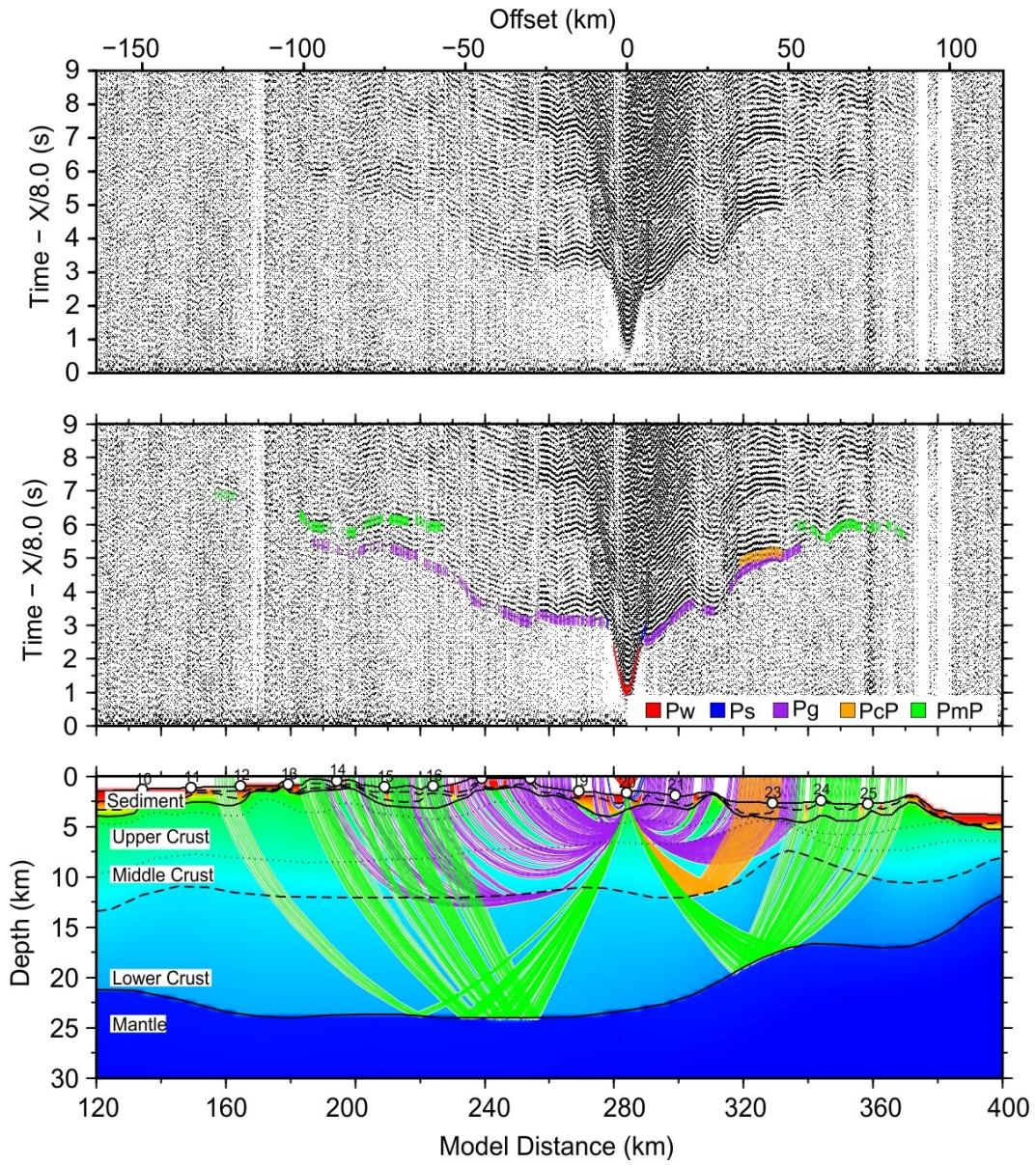


Figure S18. Seismic profile and forward modeling of OBS20

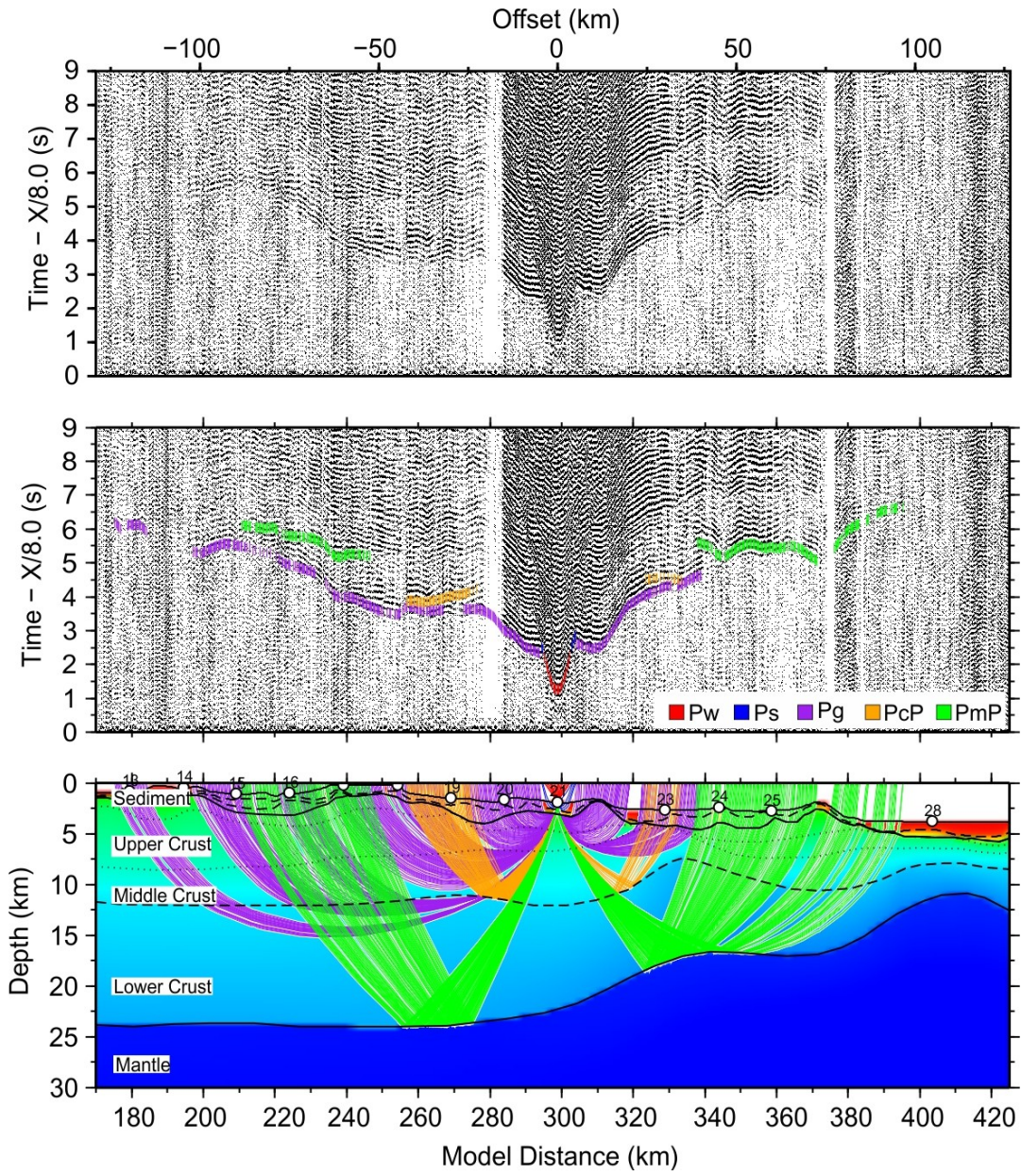


Figure S19. Seismic profile and forward modeling of OBS21

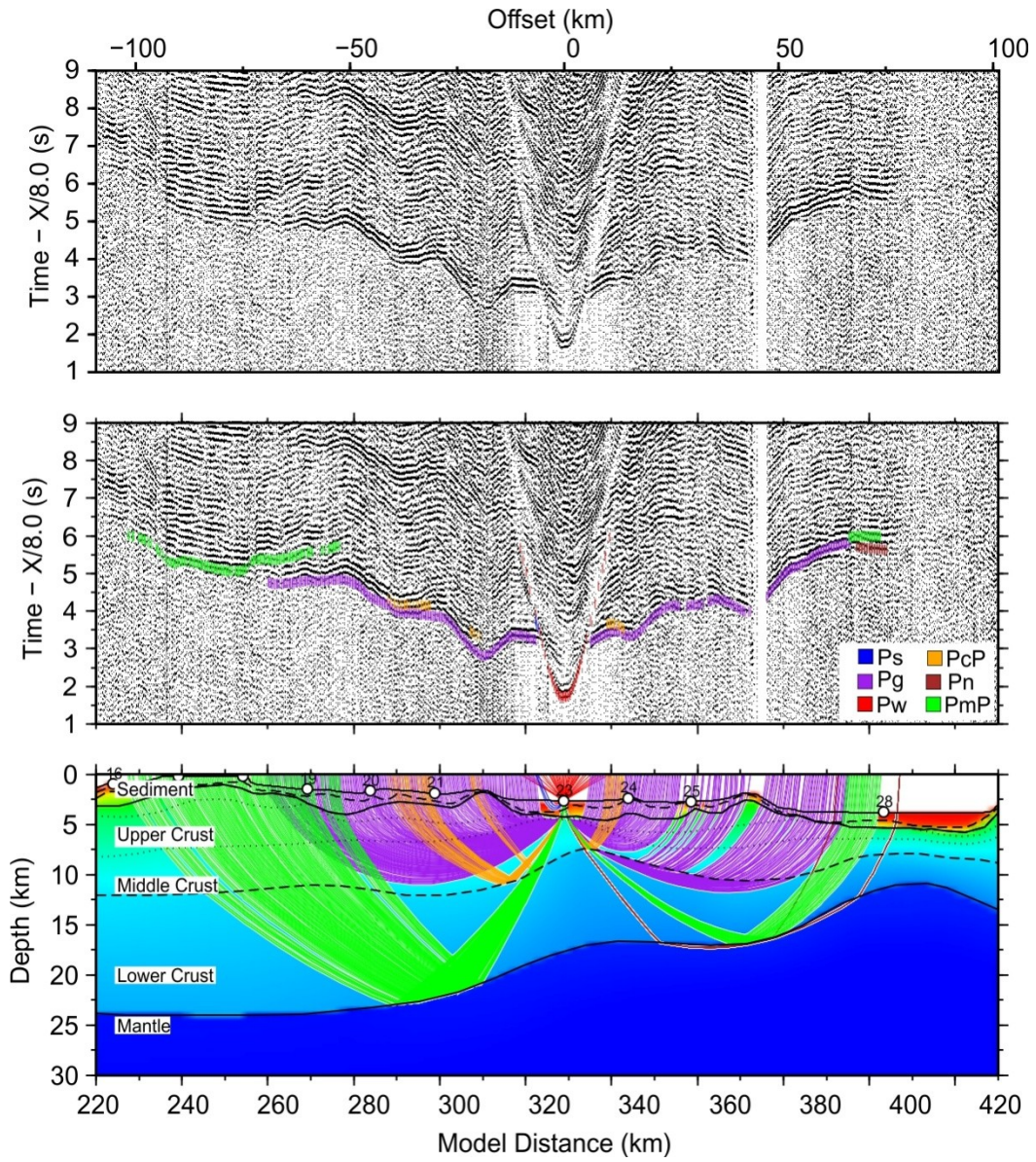


Figure S20. Seismic profile and forward modeling of OBS23

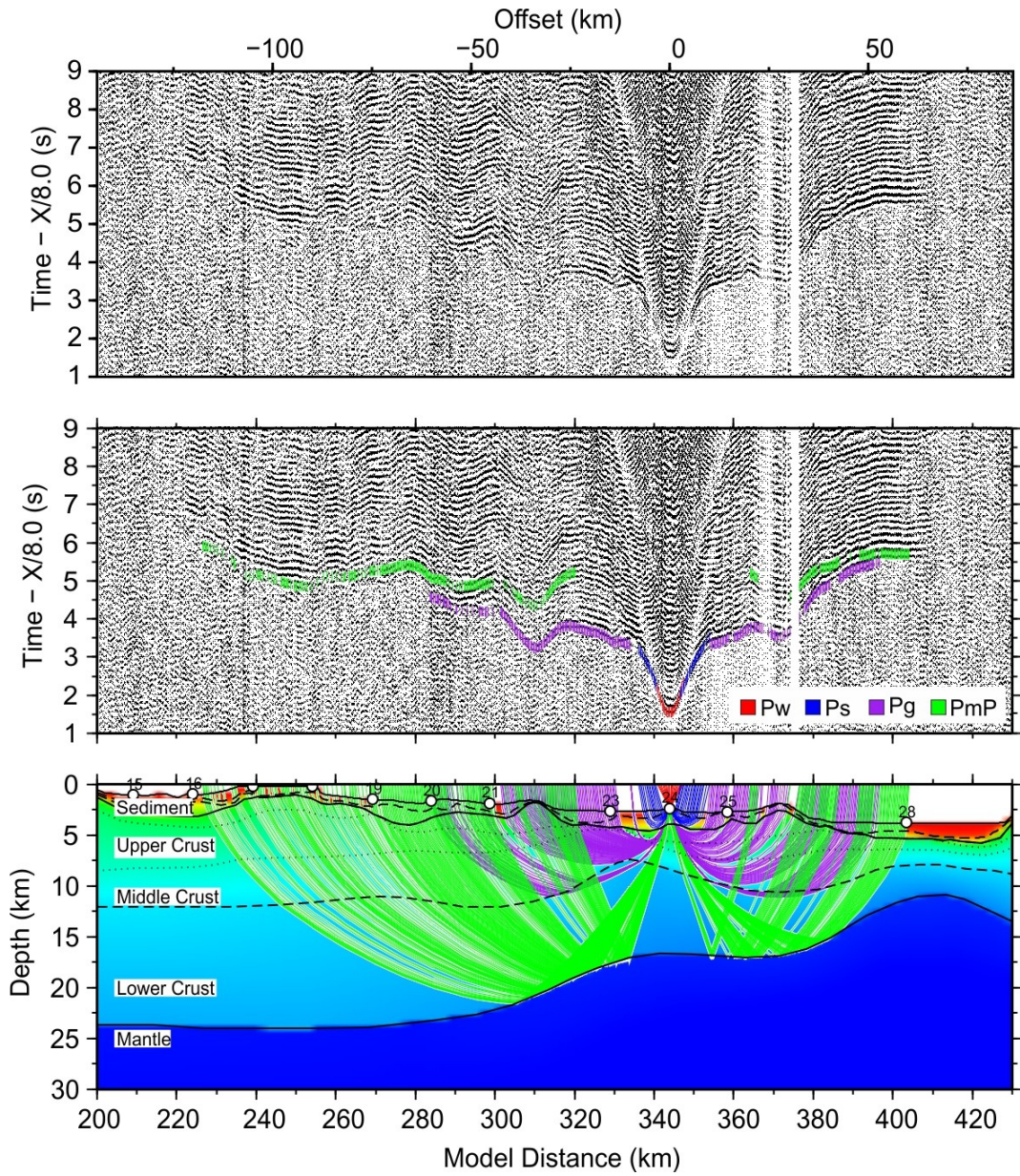


Figure S21. Seismic profile and forward modeling of OBS24

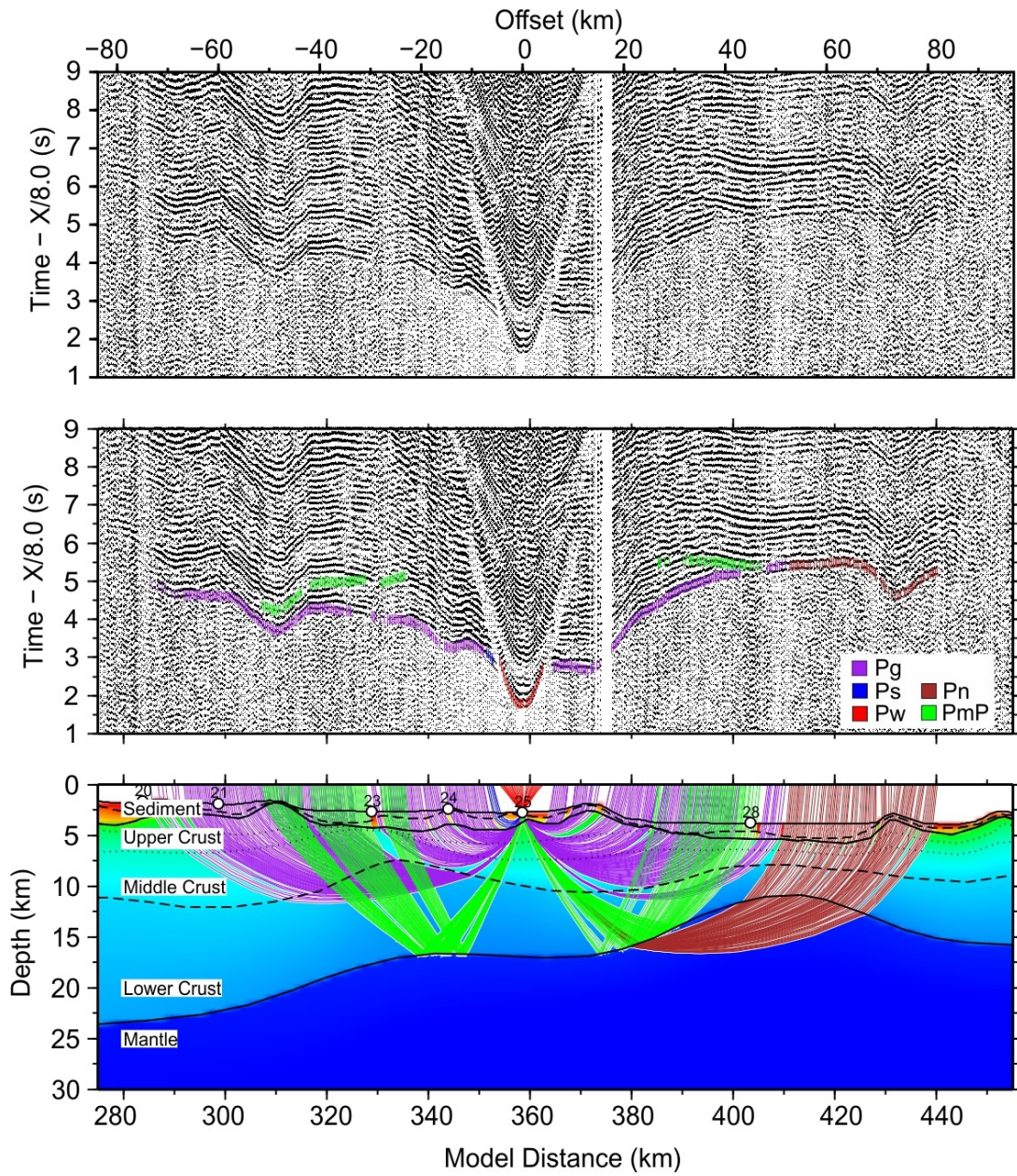


Figure S22. Seismic profile and forward modeling of OBS25

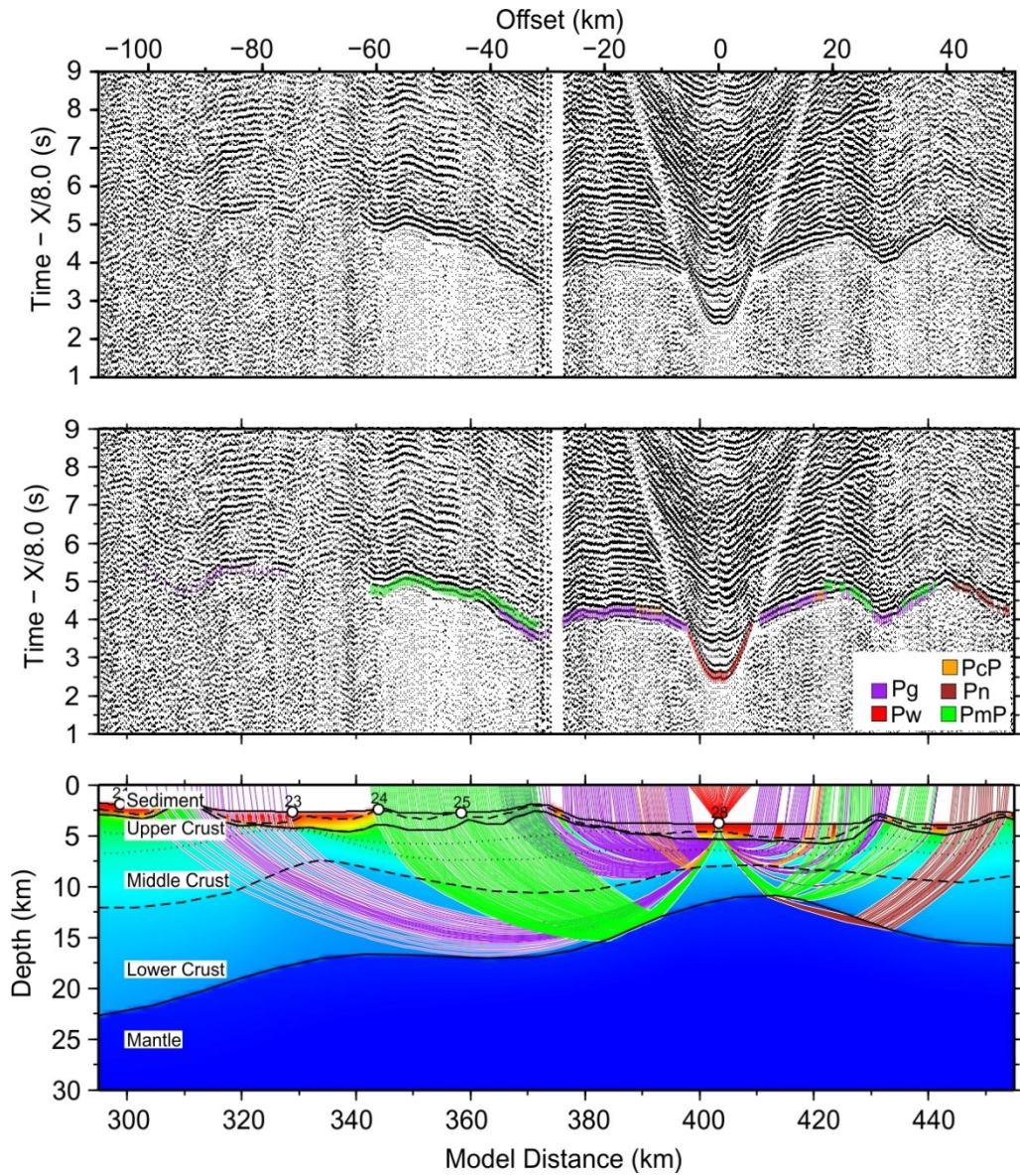


Figure S23. Seismic profile and forward modeling of OBS28